



**HAL**  
open science

## Magnetic interactions at the origin of abnormal magnetic fabrics in lava flows: a case study from Kerguelen flood basalts

Gregory Fanjat, Pierre Camps, Valera Shcherbakov, Fabrice Barou, Moulay Tahar Sougrati, Mireille M. Perrin

### ► To cite this version:

Gregory Fanjat, Pierre Camps, Valera Shcherbakov, Fabrice Barou, Moulay Tahar Sougrati, et al.. Magnetic interactions at the origin of abnormal magnetic fabrics in lava flows: a case study from Kerguelen flood basalts. *Geophysical Journal International*, 2012, 189 (2), pp.815-832. 10.1111/J.1365-246X.2012.05421.X . hal-00716449v2

**HAL Id: hal-00716449**

**<https://hal.science/hal-00716449v2>**

Submitted on 19 Oct 2020

**HAL** is a multi-disciplinary open access archive for the deposit and dissemination of scientific research documents, whether they are published or not. The documents may come from teaching and research institutions in France or abroad, or from public or private research centers.

L'archive ouverte pluridisciplinaire **HAL**, est destinée au dépôt et à la diffusion de documents scientifiques de niveau recherche, publiés ou non, émanant des établissements d'enseignement et de recherche français ou étrangers, des laboratoires publics ou privés.

# Magnetic interactions at the origin of abnormal magnetic fabrics in lava flows: a case study from Kerguelen flood basalts

G. Fanjat,<sup>1</sup> P. Camps,<sup>1</sup> V. Shcherbakov,<sup>2</sup> F. Barou,<sup>1</sup> M. T. Sougrati<sup>3</sup> and M. Perrin<sup>1,\*</sup>

<sup>1</sup>Géosciences Montpellier, CNRS and Université Montpellier 2, 34095 Montpellier, France. E-mail: camps@gm.univ-montp2.fr

<sup>2</sup>Borok Geophysical Observatory, 152742 Borok, Nekouz, Yaroslavl region, RF, Russia

<sup>3</sup>Institut Charles Gerhardt, Laboratoire des Agrégats, Interfaces et Matériaux pour l'Energie, 34095 Montpellier, France

Accepted 2012 February 13. Received 2012 February 12; in original form 2011 October 1

## SUMMARY

Anisotropy of low-field magnetic susceptibility (AMS) of basaltic lava flows can give some clues about post-emplacement tilting occurring in volcanic sequences. Such a study has been carried out on a sequence of 19 successive lava flows from Kerguelen Archipelago. Surprisingly, two different patterns were observed. The first one—herein called normal fabric—is consistent with the lava-flow direction inferred from geological observations, whereas the second one observed for about 70 per cent of the analysed samples—herein called abnormal fabric—appears to be unrelated to the shear history of the lava flows during their emplacements. These abnormal fabrics are not strictly inverse fabric but seem to have a more complex origin. The unusual nature of these abnormal fabrics has been confirmed by lattice preferred orientation of plagioclases obtained from high-resolution electron backscattered diffraction measurements. The aim of this study is to propose a physical interpretation of these fabrics. A first step in our understanding was to clearly identify the nature and the magnetic properties of the Fe-Ti oxides assemblage. Thus, we present a comprehensive rock magnetic analysis relying on low- and high-temperature thermomagnetic curves (K–T), crossover diagrams, first-order reversal curves, ore-microscopy, Mössbauer measurements and electron backscattered images. We found that in the present case the abnormal fabrics are probably linked to a mixture of prevailing single domain (SD) strongly interacting grains population and a subsidiary multidomain grains population. SD grains are identified as small magnetite crystallized within the interstitial glass in globular aggregates along the silicate framework. Then a question arises: to what extent such SD interacting grains in globular aggregates can affect the magnetic susceptibility and its anisotropy? To answer this question, we developed a physical model in which the total energy density of an SD grain with an uniaxial anisotropy is minimized. In this model, the distribution function of the direction of the magnetic interaction field is comprised between two boundary states. It is either isotropic, which formally corresponds to the thermal demagnetized state, or it is ordered, which formally corresponds to the Alternative Field demagnetized state. We show that in both cases the degree of anisotropy decreases as the interaction field increases. Thus, we conclude that the abnormal fabric encountered in this study can be simply explained by strong magnetostatic interactions that would explain the large scattering of AMS often observed in basaltic lava flows.

**Key words:** Magnetic fabrics and anisotropy; Rock and mineral magnetism; Eruption mechanisms and flow emplacement; Indian Ocean.

## 1 INTRODUCTION

When volcanic sequences present a dip, it is always difficult to tell the difference between a topographic or a tectonic origin. Do the

palaeomagnetic directions have to be tilt-adjusted before their interpretation? Linder & Leonhardt (2009) proposed a method based on the analysis of the palaeosecular variation and mean field direction to calculate numerically the palaeoslope prior to the flow emplacement. However, as they showed when applied to some icelandic volcanic sequences, this method can give an unlikely high value for the palaeoslope. A more direct alternative solution is to assess the

\*Now at: CEREGE, Europole de l'Arbois, 13545 Aix en Provence, France.

internal strain within the lava flowing over the palaeotopography from quantitative petrofabric experiments. Then, the comparison between the petrofabric-inferred flow direction and the present dip can give some indications on a possible post-emplacement tectonic tilting (Henry *et al.* 2003). A disagreement of these two directions indicates with certainty the occurrence of a significant tilting. If the two directions are similar, it is probable that no tilting occurred, keeping in mind that a tilt along the palaeoslope dip azimuth cannot be totally ruled out.

In experimental flow models, elongated particles such as laths of plagioclases interact and tend to be aligned along the flow direction (Arbaret *et al.* 1996). Nevertheless, optical microlithe orientation can be tricky to observe and thus time-consuming to measure. Anisotropy of low-field magnetic susceptibility (AMS) is more commonly used as proxy for flow direction. Easy, rapid and inexpensive to implement, this method has been successfully calibrated in basaltic lava flows with both numerous experimental studies (e.g. Cañón-Tapia 1996; Cañón-Tapia *et al.* 1996; Bascou *et al.* 2005) and analogue modellings (Hargraves *et al.* 1991; Cañón-Tapia & Pinkerton 2000). An expected model is a normal AMS fabric corresponding to a preferred orientation of non-equant-shaped magnetic grain. In this basic model, the maximum axes  $\mathbf{K}_1$  are aligned along the long axes of the grains and thus are parallel to the flow direction whereas the minimum axes  $\mathbf{K}_3$  are perpendicular to the flow plane. The imbricated fabric fixes the flow sense (Knight & Walker 1988). Distribution anisotropy, ensemble of equant- or not-equant-shaped magnetic particles distributed anisotropically and close enough to interact, will yield the same relationship between AMS and petrofabric (Hargraves *et al.* 1991; Stephenson 1994). In this case, magnetic grains are assumed to be a late-crystallizing interstitial phase within a pre-existing silicate framework. AMS carried by interacting magnetic particles mimics the silicate fabric controlled by flow forces when the magmatic flow crystallized. Distribution anisotropy is a common, if not ubiquitous, source of AMS in basaltic lava flows (Hargraves *et al.* 1991). Since the pioneering survey by Khan (1962), normal fabrics have been observed in many basaltic flows. However, Merle (1998) has shown from a mathematical analysis of 3-D experimental analogue modellings that the maximum susceptibility may under certain circumstances be perpendicular to the flow plane. Indeed, depending on the boundary conditions and strain, flow can display a magnetic fabric that does not match the flow direction. Moreover, the relationship between AMS and petrofabric can be complicated by different magnetic configurations. Cañón-Tapia & Chávez-Álvarez (2004) pointed out from a numerical modelling that the quality of the AMS fabric depends on both particle elongation and the amount of shear that is sampled. They showed in particular that two sets of particles with different aspect ratios can lead also to abnormal fabrics. Potter & Stephenson (1988) and Rochette *et al.* (1999) have shown situations where magnetic fabrics are inverse because of a predominance of single domain (SD) grains ( $\mathbf{K}_1$  perpendicular to the flow plane and  $\mathbf{K}_3$  parallel to the flow direction) and Rochette *et al.* (1999) have given examples where the magnetic fabric is intermediate between the normal and inverse models. These different observations depend on the physical origin of the AMS. It is clear that interpretation of flow direction from fabric measurement is not as straightforward as usually assumed and should always be considered in the light of both good knowledge of the magnetic mineralogy, and different strain patterns resulting from varying boundary conditions (Merle 1998).

An extensive AMS study was carried out on Kerguelen volcanic sequences (Plenier *et al.* 2002; Henry *et al.* 2003; Plenier *et al.*

2005) to decipher if the palaeomagnetic directions have to be tilt-adjusted before to be used to characterize the past Earth's magnetic field (Camps *et al.* 2007). All the sequences but one yielded coherent AMS results. Actually, in the Mount Rabouillère section, more than 70 per cent of the samples yielded a fabric that seems to be unrelated to the shear history of the lava flows. The purpose of this paper is twofold. First, we present altogether with AMS results, anisotropy of anhysteretic remanent magnetization (A-ARM) and plagioclases lattice preferred orientation (LPO) to point out the abnormal nature of these magnetic fabrics in regards with the geological context. These unusual fabrics are then discussed in the light of a comprehensive magnetic mineralogy analysis relying on microscopic images, thermomagnetic curves (K-T), crossover diagrams, Mössbauer analysis and first-order reversal curves (FORCs). Second, we present a physical model that allows us to discuss the influence of SD interacting grains, closely packed in globular aggregates, on the magnetic susceptibility and its anisotropy.

## 2 SAMPLING AND PETROLOGY

In this study, we focused on a 400-m-high section that outcrops at Mount Rabouillère in Kerguelen Archipelago, southern Indian Ocean. Along the section 19 successive flows were clearly distinguished and sampled [see Plenier *et al.* (2002) for a detailed description] as part of a large survey aiming to statistically describe the palaeomagnetic field fluctuations recorded in Kerguelen flood basalts during the late Oligocene (Camps *et al.* 2007). Therefore, the sampling was not designed strictly for AMS analysis. Six to eight oriented cores were sampled exclusively in the bottom part of each lava flow to avoid thermal remagnetization due to baking by the overlying flows. The lateral extension of the sampling along each outcrop varies from several metres to, more commonly, tens of metres. Flows are usually thin and seldom exceed 10 m in thickness. They are named from Rab1 to Rab19 in a stratigraphic order from the base to the top. This flow-on-flow sequence is subhorizontal. We estimated a very weak dip of 2–4° towards the NNE in agreement with Nougier (1970a,b)'s observations. Even though, we were aware that such a sampling was not the best for AMS analysis and may even be unsuitable if a flow scale analysis is required. Nevertheless, reliable mean flow directions have already been obtained from similar samplings on Kerguelen flood basalts by merging AMS results from three to five immediately adjacent flows (Plenier *et al.* 2002; Henry *et al.* 2003; Plenier *et al.* 2005) to decrease the large uncertainties due to the low number of sample per flow.

Major and trace element compositions and isotopic ratios of Sr, Nd and Pb of these flood basalts have been studied by Yang *et al.* (1998) along a cross-section sampled almost at the same place. The (MgO < 6 per cent) composition is transitional between alkalic and tholeiitic basalts, and no systematic variation in composition with stratigraphic height have been observed. We completed their analysis by microscopic observations from polished thin sections cut in cylinder cores with a Leitz-Orthoplan microscope ( $\times 1250$ ) in reflected and transmitted light. Lava flows are quite crystallized (about 50 per cent), with a majority of microcrysts of plagioclase and clinopyroxene. Plagioclases have a labradorite composition and a rectangular average shape of 10 over 30  $\mu\text{m}$ . Clinopyroxenes have augite composition and present sometimes phenocrysts but on average have a prismatic shape of 20 over 30  $\mu\text{m}$ . We did not observe magnetic inclusions in the augite phenocrysts. These samples contain also a few olivine phenocrysts or microcrysts partially reddish, a feature that reflects oxidation. The interstitial glass is more or

less palagonitized, indicating that a large amount of fluid played a key role in the glass formation. Opaque minerals content is usually 5–7 per cent, up to 15 per cent in some flows. In reflected-light images, large phenocrysts of ilmenite with very few large titanomagnetites as well as very small discrete opaque particles crystallized within the interstitial glass in globular aggregates can be seen. These globular aggregates have a conspicuous preferential distribution along the plagioclase laths (Fig. 1a) and their size ranges from 1 to less than 0.3  $\mu\text{m}$ . Microphotography [scanning electron microscope (SEM) image in Fig. 1b] suggests that these globules are actually clusters of several smaller particles. Zhou *et al.* (1997) observed such clusters from mid-ocean ridge basalts and identified them as titanomagnetite grains in the SD range associated with residual glass. We performed quantitative chemical analyses with a CAMECA SX100 microprobe and found that the iron content is three times larger in the globular aggregate than it is in interstitial glass. Thus, we believe that the opaque globular aggregates are made of magnetic particles although we do not have direct evidences.

### 3 MAGNETIC FABRIC VERSUS CRYSTALLOGRAPHIC FABRIC

#### 3.1 Magnetic fabric

The AMS is determined from the directional variability of the induced magnetization  $\mathbf{M}$  in an applied field  $\mathbf{H}$  where  $\mathbf{M}_i = K_{ij} \cdot \mathbf{H}_j$ . The susceptibility  $K_{ij}$  is described by a second-order tensor where the three eigenvalues  $K_1 > K_2 > K_3$  are the magnitudes of the magnetic susceptibility along a set of three orthogonal axes (eigenvectors)  $\mathbf{K}_1$ ,  $\mathbf{K}_2$  and  $\mathbf{K}_3$ , respectively (see, e.g. Tarling & Hrouda 1993, for a detailed description). To describe AMS, we used the standard parameters proposed by Jelinek (1981).

$$K_m = \frac{K_1 + K_2 + K_3}{3} \quad (1)$$

is the mean susceptibility,

$$P' = \exp \sqrt{2[(\eta_1 - \eta)^2 + (\eta_2 - \eta)^2 + (\eta_3 - \eta)^2]} \quad (2)$$

is the corrected anisotropy degree, where  $\eta = (\eta_1 + \eta_2 + \eta_3)/3$ ,  $\eta_1 = \ln K_1$ ,  $\eta_2 = \ln K_2$  and  $\eta_3 = \ln K_3$ , and

$$T = \frac{2\eta_2 - \eta_1 - \eta_3}{\eta_1 - \eta_3} \quad (3)$$

is the shape parameter. A negative value for  $T$  corresponds to a prolate shape whereas a positive value corresponds to an oblate shape. We measured AMS and mean susceptibility from one specimen per core with a susceptibility meter KLY-3S Kappabridge. A total of 109 non-demagnetized cylindrical specimens, 2.54 cm in diameter and 2.2 cm long, were analysed. Average eigenvectors were calculated for each lava flow (Table 1) by means of normalized tensors such as  $K_1 + K_2 + K_3 = 1$ , and confidence ellipses were calculated by means of both linear perturbation analysis (Hext 1963; Jelinek 1978) and bootstrap method (Constable & Tauxe 1990). Both statistics provided approximately the same results, so only Jelinek's ellipses are displayed in Fig. 2 and listed in Table 1. A large scatter in the distribution axis is observed for almost all flows (Table 1). According to Cañón-Tapia *et al.* (1997), the large variability of the magnetic fabric within lava flows requires a minimum of 10 samples to define a reliable mean flow direction. To increase the statistical significance of our AMS directions, we grouped samples from successive units yielding similar fabrics as recommended by Plenier *et al.* (2002) and Henry *et al.* (2003), even when one or

two samples have a different fabric than the average one. We did not calculate statistics at the flow level for flows Rab14 and Rab17 because they have less than four samples each, but we included their data in the group analysis. We obtained two different patterns uncorrelated to the stratigraphic position of lava flows (Table 1 and Fig. 2). We merged in Group 1 samples from lava flows yielding a consistent pattern with the flow direction inferred from geological observations (Fig. 2a). Indeed, the mean minimum axis  $\mathbf{K}_3$  presents a strong dip. The magnetic foliation plane defined by  $\mathbf{K}_1$  and  $\mathbf{K}_2$  axes is therefore close to the flow plane and the imbricated fabric fixes the flow sense northwards. Lava flows corresponding to Group 2 yield a less consistent pattern in which  $\mathbf{K}_1$  is more or less vertical (Fig. 2b). This abnormal fabric does not seem to correspond to a rigorous inverse fabric as  $\mathbf{K}_1$  and  $\mathbf{K}_3$  are not strictly switched but rather show a global rotation of the tensor. The mean direction of the principal axes is well defined for each group. AMS ellipsoids from Group 1 have rather an oblate shape whereas those from Group 2 have either an oblate or prolate shape (Fig. 2). Note that samples from Group 1 have a slightly higher mean degree of anisotropy (1.029) than these from Group 2 (1.025).

To confirm the abnormal nature of Group 2 AMS fabric and to check unambiguously the hypothesis of an inverse fabric induced by SD grains (Potter & Stephenson 1988), we measured the A-ARM on 59 samples (normal and abnormal fabrics) among the 109 used to determine AMS. The difference in the number of analysed samples is explained by the long-lasting procedure in A-ARM measurement. A cryogenic magnetometer 2G-760R, equipped with the degausser system controller 2G-600 and the anhysteretic remanent magnetizer 2G-615, was used to acquire and measure the ARM. A-ARM measurements were carried out in three steps. The samples were first demagnetized with an alternative field (AF) along three perpendicular axes with a maximum magnetic field of 170 mT. In a second time, an ARM was acquired along a direction when possible at 90° from the last demagnetized axis with a bias field between 30 and 60  $\mu\text{T}$  and AF peak values between 120 and 150 mT chosen depending on the coercivity fields of the samples. In the third step, the induced ARM was measured. These three steps were repeated for nine positions from the 15 measurements protocol of Jelinek (1976), with selected positions and the order of measurements as illustrated in Fig. 3. Similarly to AMS, A-ARM data are represented by a symmetric  $3 \times 3$  tensor whose eigenvalues  $A_1 > A_2 > A_3$  are the magnitude of the measured ARM in the three eigenvector directions,  $\mathbf{A}_1$ ,  $\mathbf{A}_2$  and  $\mathbf{A}_3$ , respectively. Measurements were grouped according to the two AMS patterns and orientations of the main axes and their mean directions were calculated (Table 2) as in AMS analysis. For the two groups, the  $\mathbf{A}_3$  axis is well defined whereas the two other axes present a girdle distribution within the foliation plane (Fig. 4). Flow direction interpretations are almost similar to those done with AMS measurements: they underline a mean flow direction from south to north. We note that measurements from Group 2 samples display a larger scattering than those from Group 1. Moreover, the orientations of principal axes present a slight rotation between the two data subsets (Fig. 4).

#### 3.2 Crystallographic fabric

We carried out measurements of LPO of plagioclases because a true inverse AMS fabric due to SD grains was not clearly identified as the cause of Group 2 abnormal fabric. Our objective was to check if some particular strain boundary conditions, as the ones pointed out in analogue modelling (Merle 1998), were present

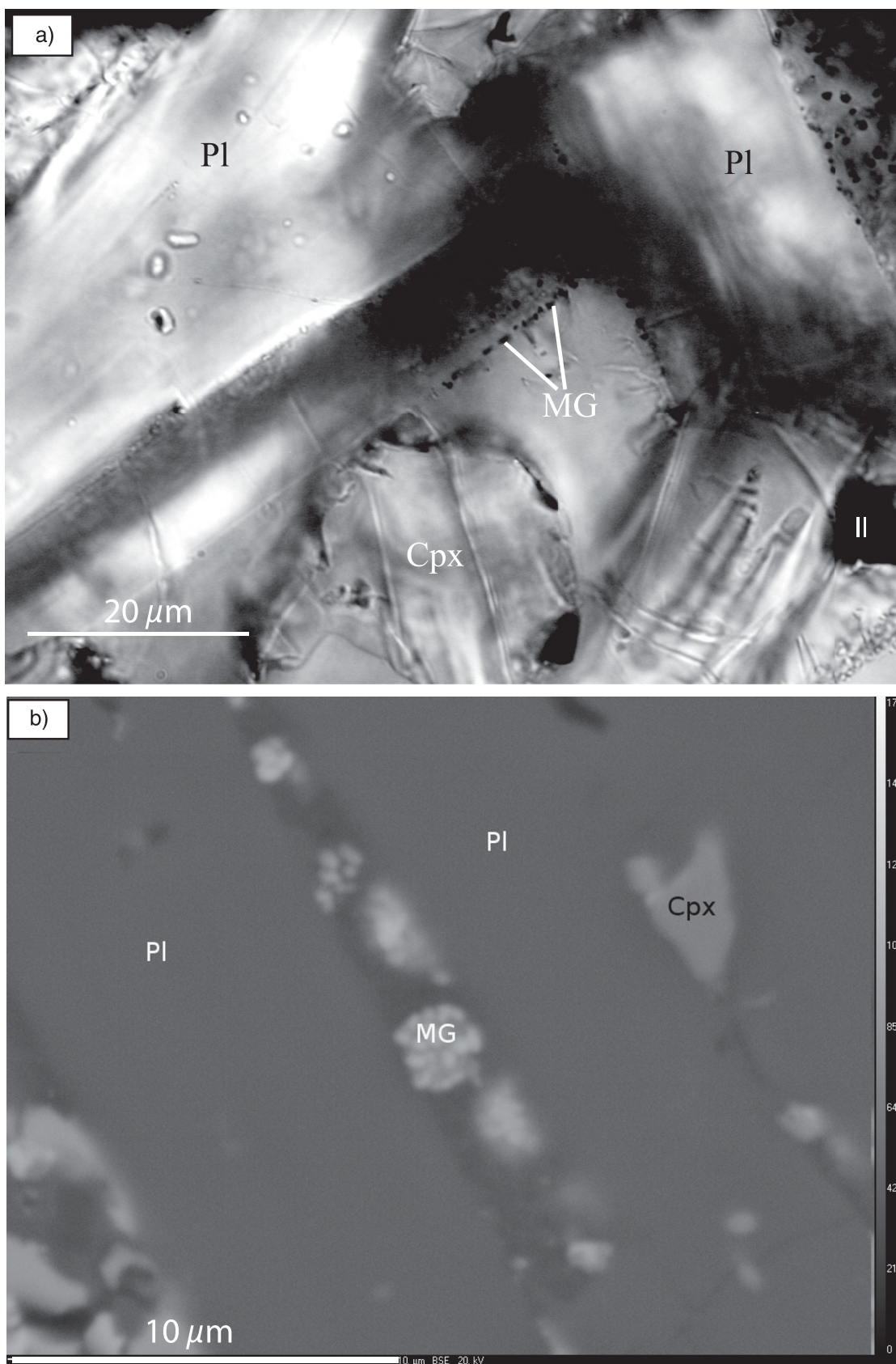


**Figure 1.** Photomicrograph of thin sections. (a) The picture of sample 00C549 (abnormal fabric) in transmitted light presents a fine microtexture with plagioclase (Pl), clinopyroxene (Cpx), titanomagnetite grains in black in interstitial glass (GI). (b) A 15-keV backscattered electron micrography from sample 00C624 (abnormal fabric) shows the same phases. Magnetite grains (MGs) are clusters of smaller particles.

**Table 1.** Mean AMS parameters.  $n$  is the number of samples per site,  $K_m$  is the mean susceptibility,  $K_1$ ,  $K_2$  and  $K_3$  are the principal axes with declination  $D(^{\circ})$  and inclination  $I(^{\circ})$ ,  $P'$  and  $T$  are the corrected degree of anisotropy and the shape parameters of the AMS ellipsoid, respectively.  $\epsilon_{ij}$  represents major and minor semi-axes angles of the uncertainty ellipses along the axes defined by the eigenvectors.  $\nu$  per cent is the geometric mean viscosity index. Lava flows marked with \* yield an abnormal AMS fabric.

| Sites                     | $n$  | $K_m$ ( $10^{-3}$ SI) | $K_1(D, I)$ | $\epsilon_{13}/\epsilon_{12}$ | $K_2(D, I)$ | $\epsilon_{23}/\epsilon_{21}$ | $K_3(D, I)$ | $\epsilon_{31}/\epsilon_{32}$ | Shape parameters |        | $\nu$ per cent |
|---------------------------|------|-----------------------|-------------|-------------------------------|-------------|-------------------------------|-------------|-------------------------------|------------------|--------|----------------|
|                           |      |                       |             |                               |             |                               |             |                               | $P'$             | $T$    |                |
| Rab19*                    | 7    | 38.8                  | 179/77      | 20/16                         | 84/1        | 44/16                         | 355/14      | 44/20                         | 1.0227           | -0.701 | 8.8            |
| Rab18*                    | 7    | 05.8                  | 332/26      | 60/44/                        | 240/4       | 84/44                         | 142/64      | 84/60                         | 1.0009           | -0.609 | 2.4            |
| Rab17*                    | 3    | n.d.                  | n.d.        | n.d.                          | n.d.        | n.d.                          | n.d.        | n.d.                          | n.d.             | n.d.   | 9.0            |
| Rab16                     | 7    | 29.1                  | 112/28      | 46/3                          | 15/12       | 46/33                         | 264/69      | 33/3                          | 1.0185           | +0.407 | 9.3            |
| Rab15*                    | 4    | 38.3                  | 153/85      | 56/37                         | 258/1       | 56/39                         | 359/5       | 39/37                         | 1.0365           | -0.128 | 13.8           |
| Rab14*                    | 1    | n.d.                  | n.d.        | n.d.                          | n.d.        | n.d.                          | n.d.        | n.d.                          | n.d.             | n.d.   | 10.7           |
| Rab13                     | 7    | 24.5                  | 125/19      | 27/8                          | 216/3       | 27/23                         | 315/71      | 23/8                          | 1.0226           | +0.357 | 4.8            |
| Rab12*                    | 5    | 20.1                  | 137/40      | 42/31                         | 280/54      | 58/42                         | 40/18       | 58/31                         | 1.0115           | -0.009 | 1.8            |
| Rab11*                    | 6    | 40.8                  | 153/70      | 27/18                         | 268/15      | 27/26                         | 22/14       | 26/18                         | 1.0277           | -0.229 | 2.6            |
| Rab10*                    | 6    | 15.5                  | 104/24      | 41/20                         | 244/59      | 61/41                         | 6/18        | 61/20                         | 1.0215           | -0.313 | 1.5            |
| Rab9*                     | 4    | 57.1                  | 52/67       | 34/33                         | 265/20      | 63/34                         | 170/11      | 63/33                         | 1.0281           | -0.192 | 23.4           |
| Rab8                      | 7    | 34.2                  | 181/38      | 61/8                          | 271/0       | 61/14                         | 1/52        | 13/8                          | 1.0389           | +0.855 | 18.3           |
| Rab7*                     | 7    | 16.4                  | 252/83      | 34/17                         | 95/16       | 34/29                         | 4/3         | 28/16                         | 1.0176           | +0.167 | 11.2           |
| Rab6*                     | 7    | 45.6                  | 135/50      | 19/12                         | 252/21      | 48/19                         | 356/32      | 48/12                         | 1.0111           | +0.050 | 4.9            |
| Rab5*                     | 6    | 41.6                  | 279/81      | 21/16                         | 157/5       | 85/21                         | 66/7        | 85/16                         | 1.0223           | -0.926 | 9.9            |
| Rab4*                     | 7    | 36.9                  | 161/47      | 56/28                         | 240/43      | 58/56                         | 67/3        | 58/28                         | 1.0122           | +0.021 | 5.7            |
| Rab3                      | 8    | 12.5                  | 162/24      | 63/28                         | 255/7       | 63/25                         | 0/65        | 28/25                         | 1.0124           | +0.582 | 0.9            |
| Rab2*                     | 6    | 12.7                  | 92/77       | 47/34                         | 270/13      | 73/47                         | 0/0         | 73/34                         | 1.0105           | -0.594 | 2.5            |
| Rab1*                     | 5    | 12.9                  | 278/61      | 41/9                          | 39/16       | 61/9                          | 137/23      | 61/41                         | 1.0241           | -0.490 | 7.8            |
| Group 1 = Normal fabric   |      |                       |             |                               |             |                               |             |                               |                  |        |                |
| 28                        | 25.1 | 129/24                | 16/5        | 225/13                        | 16/14       | 343/63                        | 16/5        | 1.0204                        | +0.497           |        |                |
| Group 2 = Abnormal fabric |      |                       |             |                               |             |                               |             |                               |                  |        |                |
| 81                        | 28.8 | 178/79                | 13/7        | 283/3                         | 14/13       | 13/11                         | 14/7        | 1.0127                        | -0.176           |        |                |

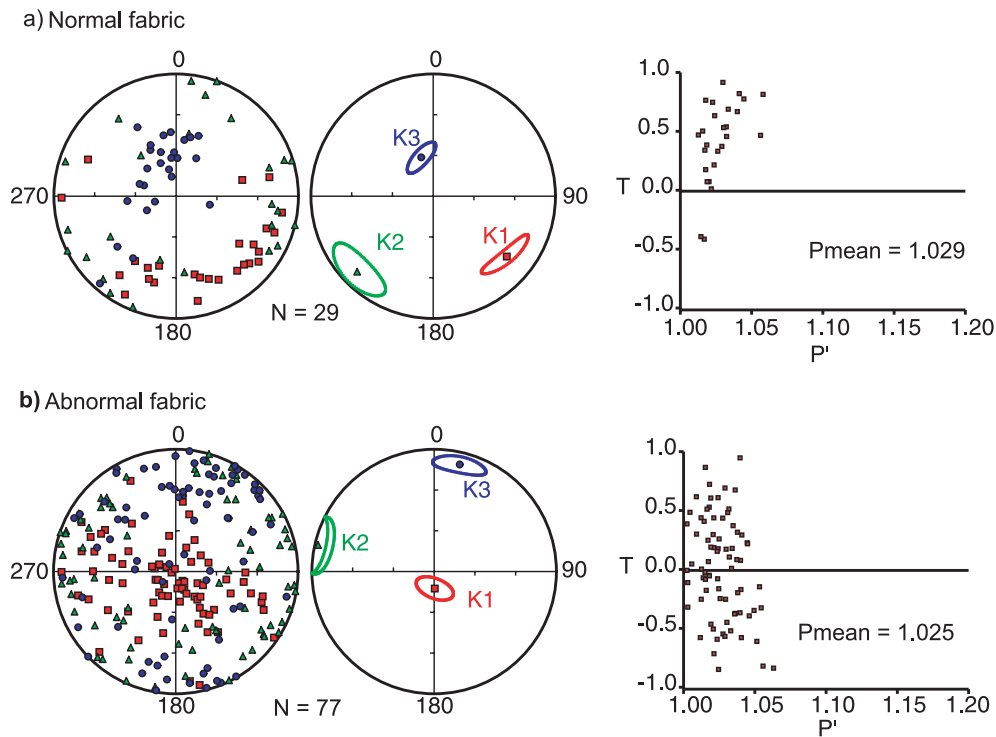


**Figure 2.** AMS fabrics, equal-area diagrams, lower hemisphere projections in geographical frame and Jelinek diagrams. (a) Samples from lava flows yielding a consistent pattern with the lava-flow direction inferred from geological observations (normal fabric). (b) Samples from lava flows yielding a less consistent pattern (abnormal fabric). In equal-area projections, squares are maximum susceptibility ( $K_1$  axes), triangles are intermediate susceptibility ( $K_2$  axes) and circles are minimum susceptibility ( $K_3$  axes). Confidence ellipses were calculated by means of Jelinek's statistics.

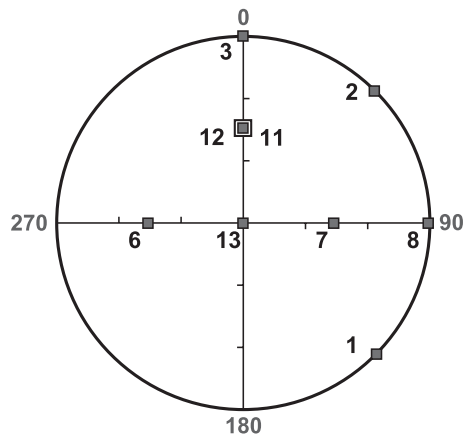


**Figure 3.** The nine measurement positions used for the acquisition of the ARM from the 15 measurement positions suggested by Jelinek (1976). Measurements are performed in the following order: 1-2-13-8-3-6-7-11-12.

during Group 2 lava flows emplacement. According to Bascou *et al.* (2005), the crystallographic fabric of plagioclases in lava flow is characterized by a strong concentration of [010] axes that defines the pole of the flow plane. Note that due to the triclinic lattice of plagioclases, [100], [010] and [001] axes do not form an orthogonal basis, whereas the axes  $K_1$ ,  $K_2$ ,  $K_3$  of the AMS ellipsoid are orthogonal. Thus, a direct comparison between LPO and AMS can only be qualitative. Oriented thin polished sections were obtained from cylindrical cores from two flows, Rab1 and Rab6 (samples 00C549 and 00C589, respectively), yielding abnormal fabrics, and from one flow, Rab8 (sample 00C606), yielding a normal fabric. LPO of plagioclases has been measured by means of the Electron BackScattered Diffraction (EBSD) with the SEM CamScan X500FE CrystalProbe of Géosciences Montpellier. Diffraction patterns were collected using the CHANNEL5 software of IJK technology (Schmidt & Olesen 1989). At each point of measurement, the Euler angles were determined with a precision better than  $1^\circ$  (Krieger-Lassen 1996). According to the mineralogical composition, we chose to measure the orientation of labradorite with the parameters defined by Wenk *et al.* (1980). For sample 00C549, we tested manual and automatic measurements. Best results were obtained for automatic sampling with a step of 50  $\mu\text{m}$ , chosen as a good compromise between the accuracy of the measurements and the surface of the analysed thin section. This sampling step did not

enable indexation of Fe-Ti oxides. We measured 18 acquisition maps (1.50 mm  $\times$  1.20 mm) for sample 00C549 (test) and 63 acquisition maps (1.20 mm  $\times$  0.9 mm) for samples 00C589 and 00C606. A good indexation quality was observed (about 40 per cent) and only measurements with a mean angular deviation (MAD) lower than  $1^\circ$  have been kept in data files. LPO statistic was analysed by Pf-ctf and ROT-ctf4 softwares. Results are displayed on equal area projection in geographical reference frame (Fig. 5). The fabric strength is expressed by the  $J$  index (Bunge 1958) which equals one for a random distribution and tends to infinity for a monocrystal. For each sample, LPO of plagioclases is characterized by a strong concentration of [010] axes (Fig. 5). The two other axes, [100] and [001], even though less concentrated, are still clustered and seem to define a plane perpendicular to the [010] direction. For the three samples, the mean [010] axis dips towards the north. Thus, whatever the magnetic fabric, the crystallographic fabric remains constant and is in agreement with the geological conclusions. The mean  $K_3$  of normal AMS fabrics points towards the same direction than the best axis of [010] whereas there is no direct correlation between  $K_3$  and [010] best axis in the case of abnormal fabrics.

## 4 MAGNETIC MINERALOGY

### 4.1 Nature of the Fe-Ti oxides

In addition to the microscopic observations, the magnetic carriers were clearly identified from K–T curves and Mössbauer spectra. First, we acquired K–T curves at low temperature with of a cryostat apparatus (CS-L) and at high temperature under Argon atmosphere with a furnace (CS-3) coupled to a KLY-3S Kappabridge instrument (Agico, Czech Republic). We analysed at least one sample per flow. Representative K–T curves obtained for samples 00C606 (flow Rab8, normal fabric), 00C579 and 00C682 (flows Rab5 and Rab19, respectively, abnormal fabric) are nearly reversible at high temperature (Fig. 6). The decrease of the magnetic susceptibility between 750 and 775 K and a Curie point near 800 K is typical of low-Ti content titanomagnetite. Low-temperature curves are not reproducible. During the first heating from liquid nitrogen temperature (78 K), the magnetic susceptibility increases with the temperature. This could indicate the presence of a mixture of multidomain (MD) and SD grains. After heating at high temperatures, the second heating from low temperatures shows a continuous decrease of the magnetic susceptibility. It is interpreted as SD grains (Senanayake & McElhinny 1982). We can infer that during heatings at high

**Table 2.** Mean A-ARA parameters. Same caption as in Table 1.

| Sites   | $n$ | $A_1(D, I)$ | $\epsilon_{13}/\epsilon_{12}$ | $A_2(D, I)$ | $\epsilon_{23}/\epsilon_{32}$ | $A_3(D, I)$ | $\epsilon_{31}/\epsilon_{13}$ | Shape parameters |         |
|---------|-----|-------------|-------------------------------|-------------|-------------------------------|-------------|-------------------------------|------------------|---------|
|         |     |             |                               |             |                               |             |                               | $P'$             | $T$     |
| Rab19*  | 6   | 250/20      | 47/15                         | 150/28      | 47/40                         | 13/556      | 42/15                         | 1.0576           | +0.570  |
| Rab13   | 7   | 125/19      | 50/10                         | 216/3       | 50/20                         | 315/71      | 19/10                         | 1.0226           | +0.357  |
| Rab11*  | 6   | 144/34      | 42/08                         | 244/15      | 42/33                         | 354/52      | 33/8                          | 1.0825           | +0.352  |
| Rab10*  | 6   | 107/29      | 38/33                         | 199/4       | 63/33                         | 296/61      | 63/38                         | 1.0414           | -0.115  |
| Rab8    | 7   | 218/29      | 22/9                          | 117/18      | 22/16                         | 1/54        | 16/9                          | 1.0801           | +0.487  |
| Rab7*   | 7   | 186/86      | 22/17                         | 292/0       | 37/22                         | 13/4        | 37/17                         | 1.0335           | -0.044  |
| Rab6*   | 7   | 164/52      | 27/20                         | 275/16      | 51/27                         | 16/34       | 51/20                         | 1.0434           | -0.056  |
| Rab3    | 8   | 223/12      | 63/22                         | 127/28      | 63/21                         | 335/61      | 22/21                         | 1.0289           | +0.789  |
| Rab1*   | 5   | 266/39      | 33/26                         | 87/51       | 70/33                         | 357/1       | 70/26                         | 1.0674           | -0.539  |
| Group 1 | 22  | 212/24      | 63/8                          | 114/18      | 63/7                          | 350/59      | 8/7                           | 1.0514           | +0.8940 |
| Group 2 | 37  | 121/34      | 66/15                         | 247/41      | 66/18                         | 8/130       | 18/15                         | 1.0258           | +0.7650 |

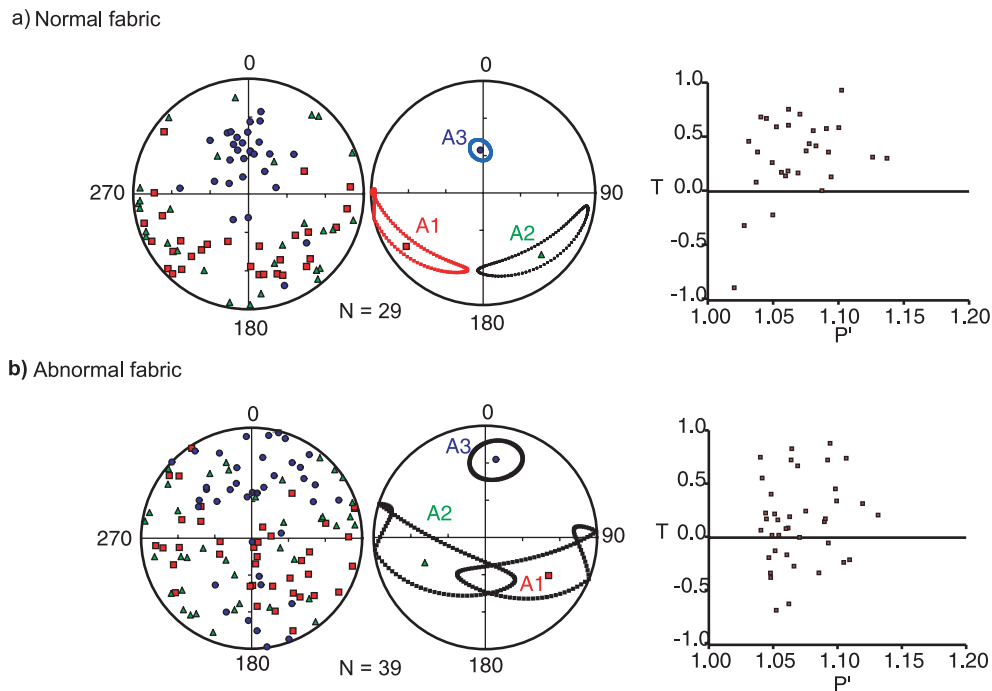


**Figure 4.** A-ARM fabrics, equal-area diagrams, lower hemisphere projections in geographical frame and Jelinek diagrams. (a) Samples from lava flows yielding a normal fabric. (b) Samples from lava flows yielding an abnormal fabric. In equal-area projections, squares are maximum ARM ( $A_1$  axes), triangles are intermediate ARM ( $A_2$  axes), and circles are minimum ARM ( $A_3$  axes). Confidence ellipses were calculated by means of Jelinek's statistics.

temperatures, oxyexsolutions of ilmenite lamellae from titanomagnetite grains occurred or continued to develop if they were already present. Whatever the magnetic fabric, the thermomagnetic curves have roughly the same behaviour.

Then, Mössbauer spectrometry was done for samples 00C563 (flow Rab3, normal fabric) and 00C561 (flow Rab2, abnormal fabric) at the Institut Charles Gerhardt, Montpellier. The spectra were recorded in transmission geometry first at room temperature with a constant-acceleration spectrometer which used a rhodium matrix  $^{57}\text{Co}$  source calibrated at 295 K with  $\alpha$ -iron foil. For this experiment, bulk rock samples have been reduced to powder in an agate mortar and sieved to keep only the size fraction lower than 50  $\mu\text{m}$ . The magnetic fraction have been concentrated from the silicate fraction in acetone by means of a magnet. The Mössbauer absorbers used in this work contained 80–100  $\text{mg cm}^{-2}$  of magnetic fraction. Velocities and isomer shift are given relative to the centre of the room temperature spectrum of  $\alpha$ -Fe foil. Spectra are displayed in Fig. 7 and the hyperfine parameters are gathered in Table 3. In spite of the magnetic separation, pyroxenes represent the most important phase in both samples. Ilmenite and magnetite spectra are also well defined in both samples even if in 00C563, ilmenite seems to have a stronger signal. According to the numerical values obtained from the fit of the Mössbauer spectra, our samples have low-Ti content ( $x < 0.1$ ) and are slightly oxidized in titanomagnhemite, according to the values obtained in the ternary diagram (Fig. 8). The presence of titanomagnhemite is in agreement with the K–T curves. Mineralogically unspecific iron(3+) is also identified. This signal can be interpreted as iron(3+) in pyroxene or a nanophase ferric oxide alteration product (Gunnlaugsson *et al.* 2008) as well as a small fraction of superparamagnetic grains (Rivas-Sanchez *et al.* 2009; Roggwiller & Kundig 1973). Assuming a continuous distribution of the size of magnetic grains and knowing the exponential nature of SD relaxation times, temperature variations may affect the Mössbauer spectra. Mössbauer spectrum at 78 K does not show any

significant modification compared to the one recorded at room temperature. A normal increase of isomer shift (Greenwood & Gibb 1971), the quadrupole splitting (Vanalboom *et al.* 1994) and the hyperfine field (Florez *et al.* 2005) has been observed. The fitted hyperfine parameters are given in Table 3. The iron (3+) does not show a magnetic order at 78 K. Similar doublets have been reported for terrestrial and martian basalts but usually not assigned (Gunnlaugsson *et al.* 2006, 2008). Thompson *et al.* (2011) have recently reported the Mössbauer spectra of a basaltic soil subjected to a gradient in precipitation. In particular, the authors found that the spectra of carbon-rich samples are mainly composed of a doublet having Mössbauer parameters in the range of the iron(3+) reported in this work. We can conclude that paramagnetic phase is then attributed to organic-iron(3+) complexes certainly coming from impurities in the acetone used to prepare the samples.

#### 4.2 Magnetite domain state and interaction field

We further checked the absence of a small population of SP grains by measuring the frequency-dependent susceptibility. Samples where SP grains are present will yield lower values of susceptibility when measured at high frequency. It is commonly accepted that frequency-dependent susceptibility values lower than 5 per cent are typical for samples in which non-SP grains dominate the assemblage. We measured the whole collection from Rabouillière with the Bartington MS2 susceptibility meter attached to the MS2B dual-frequency sensor and found that differences between values at low frequency (460 Hz) and high frequency (4600 Hz) never exceeds 3 per cent of the low-frequency value. These low values do not hold with the presence of a fraction of SP grains, and thus support our Mössbauer interpretation.

The magnetic viscosity, that is, the time dependence at a constant temperature of magnetization in a constant field, can also be



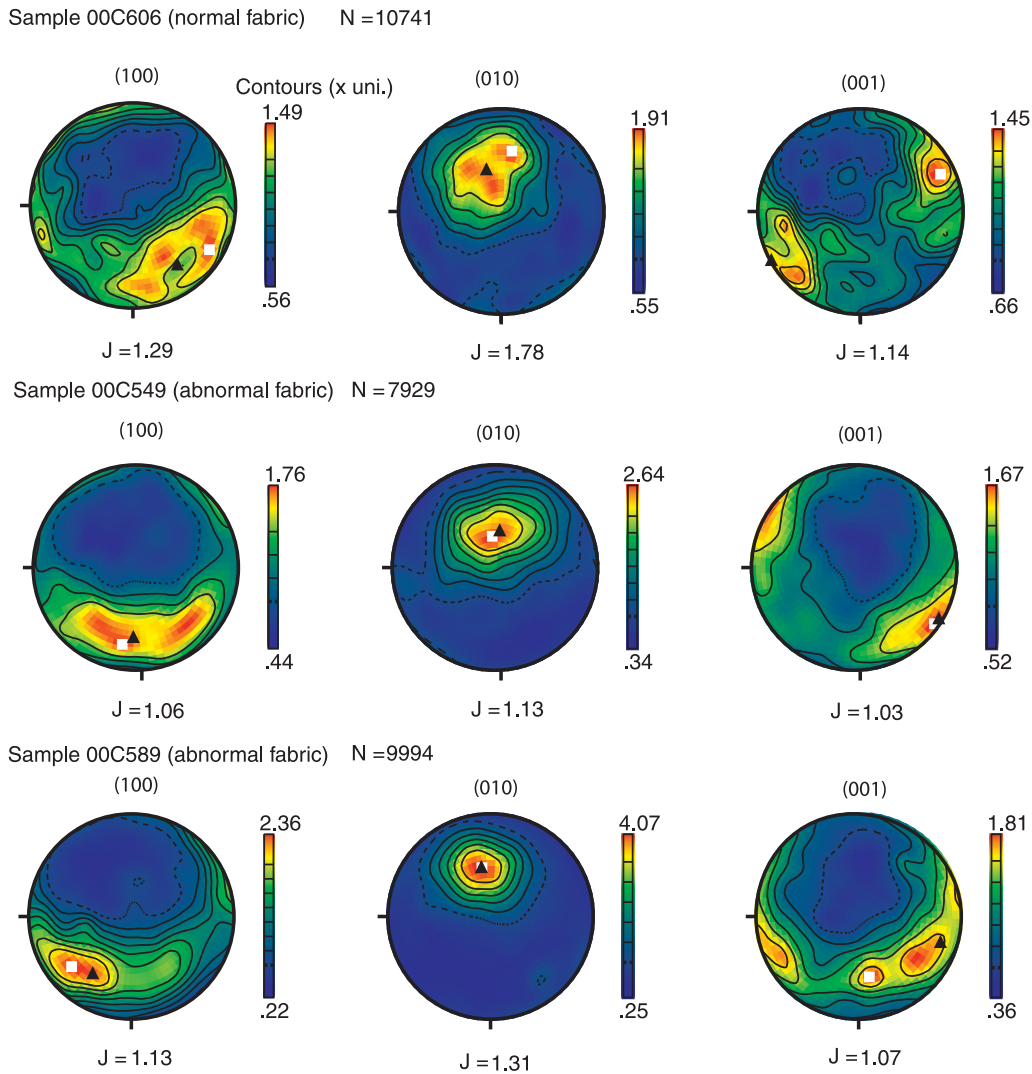


**Figure 5.** Lattice preferred orientation for samples 00C549 (Rab1), 00C589 (Rab6) and 00C606 (Rab8); Equal area projection on the lower hemisphere in geographical frame of the crystallographic axes of plagioclases. Contours are in multiples of uniform distribution.  $J$  is the texture index and  $N$  is the number of measurements for each sample. Maximum density and ‘Best Axis’ (maximum eigenvector) are represented by a square and a triangle, respectively. The dashed line is the lowest contour density.

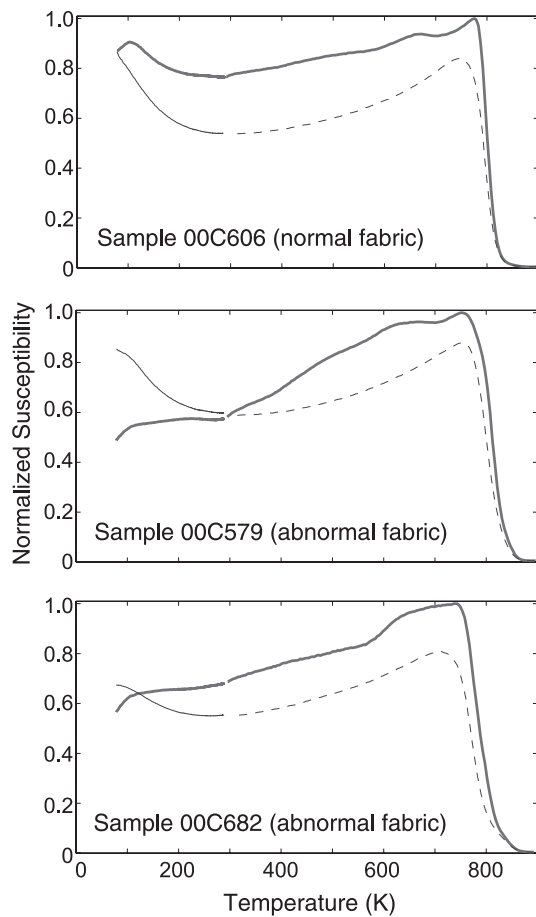
indicative of the domain state. Dunlop (1983) showed that nearly SP grains as well as large MD grains of synthetic magnetite are exceptionally viscous. We estimated the magnetic viscosity with the Thellier & Thellier (1944)’s 2-week viscosity index ( $\nu$ ). In this test, room-temperature acquisition and decay of a small viscous magnetization are estimated by measuring the remanent magnetization first after 2 weeks of storage with the ambient field parallel to the positive  $z$ -axis of each specimen ( $\vec{M}_1$ ), and then after another 2-week storage in zero-field ( $\vec{M}_2$ ). This index is expressed in per cent by

$$\nu = \frac{|\vec{M}_1 - \vec{M}_2|}{|\vec{M}_2|} \times 100.$$

For all lava but two, Rab8 (normal fabric) and Rab9 (abnormal fabric), the viscosity indexes averaged by flow are more or less comparable to the mean value of 6.1 per cent found for some upper tertiary and pre-Bruhnes quaternary subaerial volcanic rocks (Prévoit 1981) (Table 1). The high values of 18.3 and 23.4 per cent found for Rab8 and Rab9 units, respectively, could reflect the pres-

ence of a significant fraction of very small SD or large MD grains in these two flows.

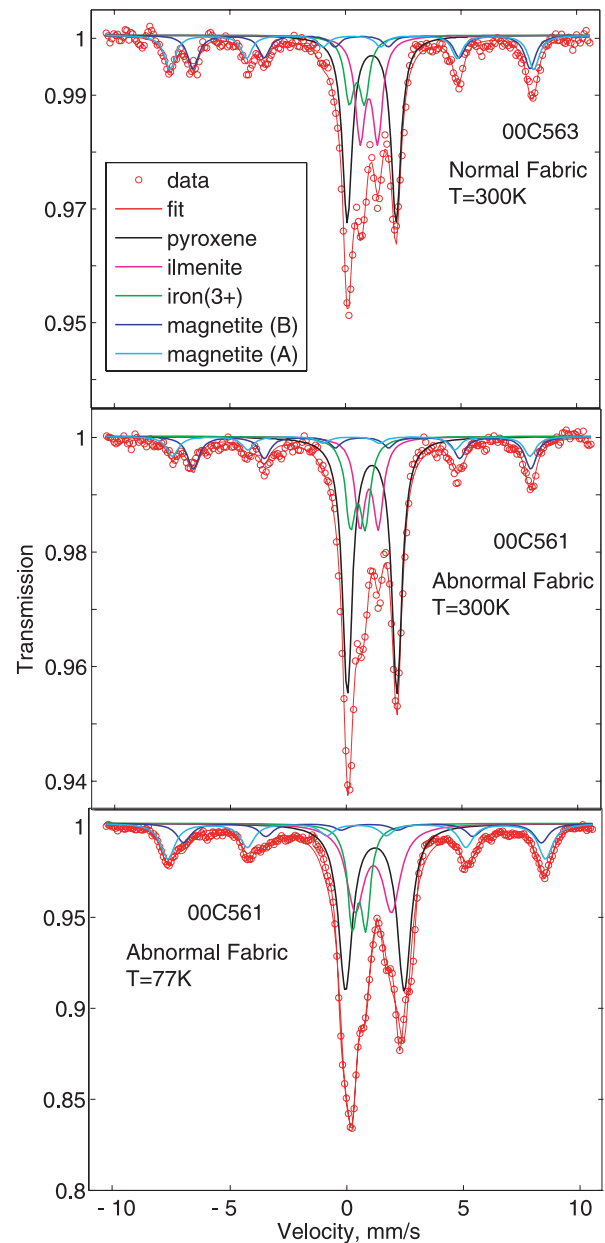
Crossover diagrams (Cisowski 1981), plot of acquisition and demagnetization of isothermal remanent magnetization (IRM), demonstrate the presence of SD interacting grains. Indeed, interaction fields between SD grains shift the coercivity spectrum to lower values for AF demagnetization and to higher values for IRM acquisition. The intersection point projected on the abscissa approximates the remanent coercive force  $H_{RC}$ . Wohlfarth (1958) showed that the  $R$  ratio ( $R = IRM(H_{RC})/IRM(\max)$ ) is equal to 0.5 for non-interacting magnetic SD grains and is lower than 0.5 for interacting grains. We performed crossover diagrams (Fig. 9) on three samples from flows yielding an abnormal fabric, 00C549 (Rab1), 00C586 (Rab6) and 00C637 (Rab13), and on one sample from a normal fabric flow, 00C603 (Rab8). The acquisition curve has been obtained by measuring with the JR5 spinner magnetometer an IRM induced with the ASC Magnetizer from 0 to 250 mT along the  $z$ -axis of a mini-core (1 cm in diameter and 1 cm long). The demagnetization curve has been obtained by stepwise AF treatment with peak values in the same range than the acquisition curve. All



**Figure 6.** Thermomagnetic curves at low and high temperature. The first heating from liquid nitrogen temperature (78 K) is the thick black curve and the second heating is the fine grey curve. The dashed line is the cooling part of the experiment.

samples present an asymmetrical acquisition curve compared to the demagnetization curve:  $R$  values range between 0.2 and 0.35. These results substantiate the presence of SD interacting grains and/or MD grains, the  $R$  ratio being unfortunately unable to differentiate the two possibilities. However, samples dominated by MD grains can be distinguished from interacting SD grains in how fast they saturate. Indeed, samples with MD will show steeper IRM acquisition curves at low fields, as the sample 00C603 (normal fabric) which shows a steeper acquisition and a quicker demagnetization than the other samples. This observation, together with the high-viscosity index measured in this flow, supports the presence of a significant fraction of MD grains in flow Rab8 (normal fabric).

FORC diagrams will bring more precise information about the origin of the magnetic interactions. They are constructed by measuring a large number of partial magnetic hysteresis curves known as first-order reversal curves or FORCs, and they are represented by contour plot of 2-D distribution functions ( $H_c, H_b$ ) (Pike *et al.* 1999) where  $H_c$  provides indirect information about the magnetic domain structure and  $H_b$  gives information about magnetostatic interactions. A first interpretative framework of FORC diagrams in terms of magnetic domain states was given by Roberts *et al.* (2000). We measured FORCs for one sample from each flow with the Micro Vibrating Sample Magnetometer of the CEREGE institute (Aix en Provence, France). Fig. 10 shows representative FORCs diagrams obtained from normal and abnormal fabric flows, respectively. The

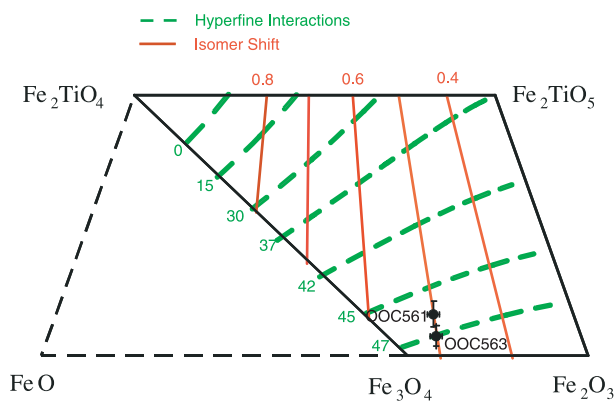


**Figure 7.** Room temperature Mössbauer spectra for samples 00C563 (normal fabric) and 00C561 (abnormal fabric). Fittings components for pyroxene, ilmenite, magnetite site A and B and unspecific iron(3+) are displayed.

large-scale FORC diagrams (Figs 10a and c) of the 00C606 and 00C626 samples share more similarities than can be seen from the zoomed diagrams (Figs 10b and d). Yet, there are important differences: Compared to 00C626, sample 00C606 has a more pronounced reversible ridge and a less distinct coercivity maximum at 10 mT and therefore is a ‘softer’ Pseudo-Single Domain (PSD) sample, that is, a PSD that is closer to MD, which is consistent with a normal fabric. Sample 00C626 does have a nicely isolated coercivity maximum at 10 mT, which is consistent with strongly interacting magnetite particles. However, viscous SD particles that have a relaxation time of the order of the measurement timescale, that is, 0.1–1 s, may seem similar to MD behaviour on FORCs spectra. However, according to our previous observations and conclusions from Mössbauer spectra, frequency-dependent susceptibility and viscosity index, Figs 10a and b are interpreted as MD grains. On

**Table 3.** Parameters obtained from the analysis of Mössbauer spectra of samples 00C563 and 00C561. IS is the isomer shift, QS is the quadrupole splitting, LW is the line width and HF is the hyperfine field.

|  | IS (mm s <sup>-1</sup> ) | QS (mm s <sup>-1</sup> ) | LW (mm s <sup>-1</sup> ) | HF (T)       | Contribution (per cent) |
|--|--------------------------|--------------------------|--------------------------|--------------|-------------------------|
| 00C561 (Normal fabric), Room temperature   |                          |                          |                          |              |                         |
| Pyroxene                                   | 1.12 ± 0.01              | 2.14 ± 0.01              | 0.53 ± 0.01              | 0.00         | 47 ± 4                  |
| Ilmenite                                   | 0.99 ± 0.01              | 0.79 ± 0.03              | 0.53 ± 0.01              | 0.00         | 16 ± 1                  |
| unspecified Fe(III)                        | 0.50 ± 0.02              | 0.64 ± 0.03              | 0.53 ± 0.01              | 0.00         | 15 ± 1                  |
| Magnetite (A)                              | 0.22 ± 0.06              | 0.00                     | 0.61 ± 0.08              | 47.93 ± 0.46 | 9 ± 1                   |
| Magnetite (B)                              | 0.68 ± 0.04              | 0.00                     | 0.61 ± 0.08              | 45.23 ± 0.29 | 14 ± 1                  |
| 00C561 (Normal fabric), 77 K               |                          |                          |                          |              |                         |
| Pyroxene                                   | 1.20 ± 0.00              | 2.52 ± 0.01              | 0.72 ± 0.01              | 0.00         | 37 ± 3                  |
| Ilmenite                                   | 1.14 ± 0.01              | 1.56 ± 0.03              | 0.91 ± 0.01              | 0.00         | 24 ± 1                  |
| unspecified Fe(III)                        | 0.53 ± 0.00              | 0.58 ± 0.01              | 0.49 ± 0.01              | 0.00         | 16 ± 1                  |
| Magnetite (A)                              | 0.22 ± 0.06              | 0.00                     | 0.61 ± 0.08              | 50.23 ± 0.08 | 16 ± 1                  |
| Magnetite (B)                              | 0.68 ± 0.04              | 0.00                     | 0.61 ± 0.08              | 47.58 ± 0.15 | 9 ± 1                   |
| 00C563 (Abnormal fabric), Room temperature |                          |                          |                          |              |                         |
| Pyroxene                                   | 1.13 ± 0.01              | 2.11 ± 0.03              | 0.51 ± 0.02              | 0.00         | 37 ± 6                  |
| Ilmenite                                   | 1.01 ± 0.01              | 0.75 ± 0.03              | 0.51 ± 0.02              | 0.00         | 20 ± 1                  |
| unspecified Fe(III)                        | 0.49 ± 0.05              | 0.65 ± 0.08              | 0.51 ± 0.02              | 0.00         | 12 ± 1                  |
| Magnetite (A)                              | 0.28 ± 0.04              | 0.00                     | 0.57 ± 0.07              | 48.83 ± 0.26 | 15 ± 2                  |
| Magnetite (B)                              | 0.70 ± 0.04              | 0.010                    | 0.57 ± 0.07              | 45.25 ± 0.28 | 15 ± 2                  |

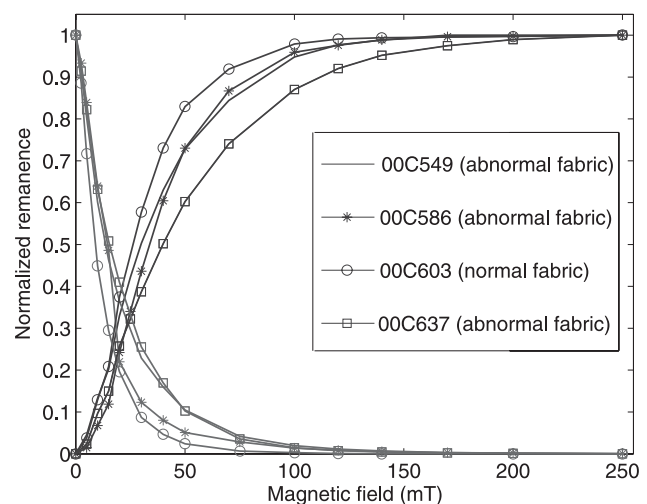
**Figure 8.** Contours of constant average magnetic hyperfine field and average isomer shift as determined by room-temperature Mössbauer spectroscopy in the FeO-TiO<sub>2</sub>-Fe<sub>2</sub>O<sub>3</sub> ternary system (Gunnlaugsson *et al.* 2008) for the samples 00C561 and 00C563.

the contrary, closed curves (Fig. 10d) obtained for samples yielding an abnormal fabric are related to SD grains (Roberts *et al.* 2000), the large dispersion along  $H_b$  being interpreted as strongly interacting SD grains (Pike *et al.* 1999; Egli 2006b; Evans *et al.* 2006).

## 5 DISCUSSION

To sum up the experimental study, we demonstrated that the abnormal magnetic fabrics measured in the Mount Rabouillère volcanic sequence is not simply an inverse fabric due to SD grain population, but is rather related to a mixture of prevailing SD interacting grains population and a subsidiary MD grains population. SD grains were clearly identified as small titanomagnetite crystallized within the interstitial glass in globular aggregates, not uniformly distributed within the matrix but aligned along the plagioclase laths. Now the question is: to what extent such SD interacting grains can affect the magnetic susceptibility and its anisotropy?

An important parameter controlling the interaction field intensity is the packing parameter  $p$ . Indeed, the closer the SD particles

**Figure 9.** Crossover diagrams for the samples 00C549, 00C586, 00C637 (abnormal fabric) and 00C607 (normal fabric): magnetization and demagnetization curves (normalized to the maximal magnetization) as a function of the applied alternative field (mT).

are, the stronger the interaction field is. The mean size of these clusters is about 0.3–0.5  $\mu\text{m}$ . The size for SD magnetite grains is 0.03–0.05  $\mu\text{m}$  (Dunlop & Özdemir 1997). Considering an ensemble of spheres, for example, SD magnetite grains, which are packed, the packing parameter or the relative volume  $p$  of the magnetic particles is defined by the ratio between the total volume of the cluster and the volume occupied by the particles. Numerical simulations show that the maximal packing parameter for random close packing spheres is 0.636 (Torquato *et al.* 2000). According to the size of the cluster and the size of the SD particles, we suggest two scales of packing: SD particles packed in small clusters of about 0.1  $\mu\text{m}$ , further packed in a bigger cluster. Thus, we evaluated for the globular aggregates observed a maximum packing parameter between 0.20 and 0.40. The presence of strongly interacting SD particles in abnormal fabrics

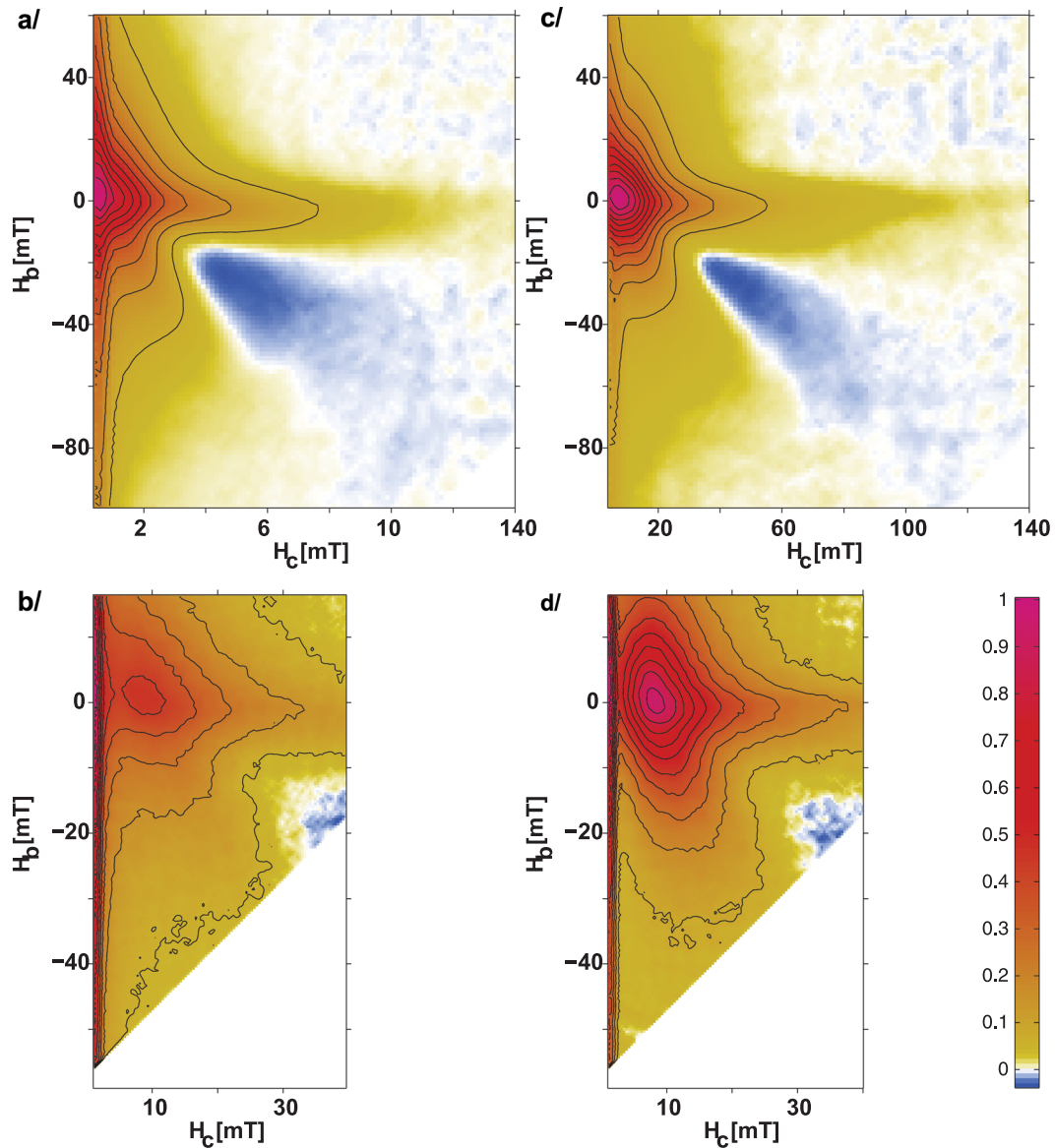


**Figure 10.** FORC diagrams processed by the Winklhofer & Zimany (2006)'s Matlab code. (a) large-scale and (b) zoomed FORCs diagrams for sample 00C606 yielding a normal fabric; (c) large-scale and (d) zoomed FORCs diagrams for sample 00C626 yielding an abnormal fabric. Smoothing factor (SF) = 3 for all plots.

samples will likely alter the AMS signal. To check this hypothesis, we developed a physical model to test the influence of magnetic interactions on magnetic susceptibility and its anisotropy.

The theoretical study of role of magnetostatic interactions on magnetic susceptibility has been initiated by Stephenson (1994) who showed that magnetically isotropic particles with linear or planar regular arrangements give rise to the AMS. Cañón-Tapia (1996) and Gaillot *et al.* (2006) generalized this model by studying the effects of individual-particle anisotropy in the AMS. However, the main drawback of these models is that they always suggest a regular arrangement of magnetic particles in a sample. Obviously, in reality it is not true that the grains are actually randomly distributed over the volume of a specimen. As a consequence, the magnetic fields generated by these grains are also random and therefore their effect on AMS can be drastically different from those of regularly ordered interaction fields generated by regularly arranged particles. The purpose of the last part of the study is to develop an appro-

priate theoretical model accounting for the random character of the interaction fields.

### 5.1 Numerical approach

The natural way to model systems of interacting particles is to introduce the local interaction field  $H_{int}$ . For a given grain, this field is produced by all the other grains in the cluster. As the grains are randomly distributed over the volume of the cluster, the intensity of the local interaction fields is also random and can be described statistically with a probability density function  $W(H_{int})$ . For the densely packed cluster, this function can be approximated by a Gaussian distribution (Shcherbakov & Shcherbakova 1975; Egli 2006b).

$$W(H_{int}) = \frac{1}{\sigma_0 \sqrt{2\pi}} \exp\left(-\frac{H^2}{2\sigma_0^2}\right) \quad (4)$$

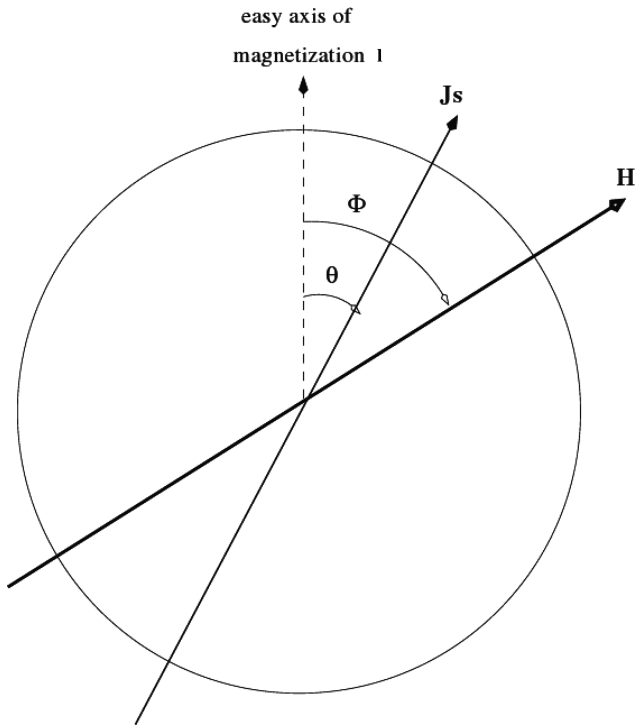


**Figure 11.** Sketch of a possible influence of magnetostatic interactions on an uniaxial SD particle.  $\mathbf{J}_s$  is the spontaneous magnetization,  $\mathbf{H}$  is the interaction field and  $\phi$  the angle between  $\mathbf{H}$  and  $\mathbf{l}$ .

with the dispersion  $\sigma_0 = 0.3J_s\sqrt{p}$ , and  $J_s$  is the saturation magnetization of grains. For  $J_s \approx 480 \text{ kA m}^{-1}$  (magnetite) at  $p \approx (0.2-0.4)$ , the dispersion  $\sigma_0$  reaches values on the order of 100 mT. That means that the local fields can be really strong in accordance with the results inferred from the FORCs diagrams and the Cisowski's test.

### 5.1.1 Magnetic energies for SD particles with uniaxial anisotropy

Consider an SD particle with an uniaxial anisotropy and a spontaneous magnetization  $\mathbf{J}_s$  and let be  $\theta$  the angle between  $\mathbf{J}_s$  and the easy axis of magnetization  $\mathbf{l}$ . If magnetostatic interactions are neglected and no external magnetic field is applied, the magnetic moment is aligned with  $\mathbf{l}$ . However, under the influence of magnetostatic interactions  $\mathbf{H}$ ,  $\mathbf{J}_s$  is deflected from the easy axis with an angle  $\theta$  (Fig. 11).

The total energy  $E_{\text{tot}}$  of the grain is (see e.g. O'Reilly 1984)

$$E_{\text{tot}} = E_{\text{an}} + E_{\text{int}}, \quad (5)$$

where

$$E_{\text{an}} = K \sin^2 \theta \quad (6)$$

is the anisotropy energy and

$$E_{\text{int}} = -\mathbf{J}_s \cdot \mathbf{H}_{\text{int}} \quad (7)$$

is the magnetostatic interaction energy. Here, the dimensionless non-perturbed energy density is

$$E_0 = \sin^2 \theta - H \cos(\phi - \theta), \quad (8)$$

where  $H$  is a dimensionless interaction magnetic field ( $H = J_s H_{\text{int}}/K$ ). For the following study, the interaction magnetic field  $H$  is a proxy of the packing parameter, as stated earlier by eq. (4), and can be estimated in natural samples by microscopic observations.

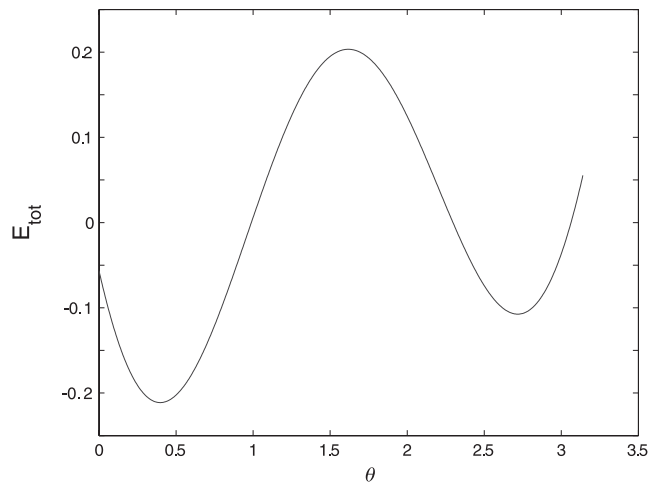


**Figure 12.** The total energy density  $E_{\text{tot}}$  as a function of the angle  $\theta$  for  $H = 0.8$  and  $\psi = 1.5$  (cf. eq. 10).

The position of equilibrium  $\theta_0$  of the magnetic moment corresponds to the minimum of  $E_0$ . This position is found by solving

$$\frac{\partial E_0}{\partial \theta} = \sin(2\theta) - H \sin(\phi - \theta) = 0. \quad (9)$$

The roots  $\theta_0$  depend on the value of  $\phi$ ,  $\phi \in [-\pi; \pi]$ . For  $H < 1$ , there are always two minima states of the energy:  $\theta_0^1$  and  $\theta_0^2$ , where  $\theta_0^1$ , corresponding to  $\phi < \pi/2$ , is the deep potential well whereas  $\theta_0^2$ , corresponding to  $\pi/2 < \phi < \pi$ , is the shallow potential well (Fig. 12).

In this geometry, consider that the SD particle is submitted to a small external field  $h_{\text{small}}$  as  $h_{\text{small}} \ll H_{\text{int}}$  (susceptibility measurement for example). The total energy density  $E_{\text{tot}}$  becomes

$$E_{\text{tot}} = E_0 - \Delta E = \sin^2(\theta) - H \cos(\theta - \phi) - h \cos(\theta - \psi), \quad (10)$$

where  $\psi \in [-\pi; \pi]$  is the angle between small field  $\mathbf{h}$  and the axis of easy magnetization and  $h = J_s h_{\text{small}}/K$  is dimensionless magnetic field. For simplicity, consider here the 2-D arrangement when the easy axis and the fields  $\mathbf{H}$  and  $\mathbf{h}$  lay in the same plane. The generalization for the 3-D case is straightforward but bulky and is presented elsewhere (Fanjat *et al.* 2012). In this case, the position of equilibrium is slightly deflected from its initial position by a small angle  $y$ . So  $\theta'_0 = \theta_0 + y$  where  $y \ll 1$ . The development of  $E_{\text{tot}}$  in Taylor's series at  $\theta'_0$  (eq. 11) gives an expression of  $E_{\text{tot}}$  in terms of  $F$ , the second derivative of  $E_0$  (eq. 12).

$$E_{\text{tot}}(\theta_0 + y) \approx F \frac{y^2}{2} - h \cos(\psi - \theta_0 - y) + cst, \quad (11)$$

$$F = \frac{\partial^2 E_0}{\partial \theta^2} = 2 \cos(2\theta) + H \cos(\phi - \theta). \quad (12)$$

The expression of the induced magnetic moment  $m_{\text{ind}}$  is obtained by the projection of this equation on  $\mathbf{h}$  when  $\phi$  and  $\psi$  are given

$$\begin{aligned} m_{\text{ind}}(\psi) &= J_s \cos(y + \theta_0 - \psi) \\ &= J_s \cos(\theta_0 - \psi) + \frac{J_s}{F} h \sin^2(\theta_0 - \psi). \end{aligned} \quad (13)$$

The total induced magnetic moment is obtained by the integration of eq. (13) over  $\phi$  and  $\psi$ . As is seen from eq. (13), the intensity of the induced magnetization is inversely proportional to the value of the second derivative  $F$ , which means that the susceptibility increases with the increase of the interaction field  $H$  for the shallow potential well  $\pi/2 < \phi < \pi$  and decreases inside the deep potential

well  $0 < \phi < \pi/2$ . The following scenario depends on the initial magnetization state of the sample. Whatever is the nature of the remanent magnetization in a natural sample, the distribution function of the interaction field is comprised between two boundary states: either isotropic, which formally corresponds to the thermal demagnetized state, or strongly ordered, which formally corresponds to the AF-demagnetized state.

### 5.1.2 Isotropic distribution for the easy axes

*Thermodemagnetized state.* Let us consider now that we have a sample for which the distribution function for  $\mathbf{H}$  is isotropic. Then, introducing the blocking temperature  $T_b$  of a grain, the probability that  $\theta_0$  belongs to either  $\theta_0^1$  or  $\theta_0^2$  is described by the Boltzman's distribution

$$P[\theta_0^i(\phi)] = \frac{1}{C} e^{-\frac{E_0[\theta_0^i(\phi)]}{k_B T_b}} \quad \text{for } i = (1,2), \quad (14)$$

where

$$C = e^{-\frac{E_0[\theta_0^1(\phi)]}{k_B T_b}} + e^{-\frac{E_0[\theta_0^2(\phi)]}{k_B T_b}} \quad (15)$$

and  $k_B$  is the Boltzman's constant. The total magnetic moment can be found by averaging eq. (13) over  $\phi$  and  $\psi$ .

$$\begin{aligned} M = & \frac{1}{2C\pi^2} \left( \int_{-\pi/2}^{\pi/2} \int_{-\pi}^{\pi} (\cos(\theta_0 - \psi) \right. \\ & \left. + h \frac{\sin^2(\theta_0 - \psi)}{F} \right) f(\phi, \psi) d\psi e^{-\frac{E_0^1(\phi)}{k_B T_b}} d\phi \\ & + \int_{\pi/2}^{\pi} \int_{-\pi}^{\pi} (\cos(\theta_0 - \psi) \\ & \left. + h \frac{\sin^2(\theta_0 - \psi)}{F} \right) f(\phi, \psi) d\psi e^{-\frac{E_0^2(\phi)}{k_B T_b}} d\phi \\ & + \int_{-\pi}^{-\pi/2} \int_{-\pi}^{\pi} (\cos(\theta_0 - \psi) \\ & \left. + h \frac{\sin^2(\theta_0 - \psi)}{F} \right) f(\phi, \psi) d\psi e^{-\frac{E_0^2(\phi)}{k_B T_b}} d\phi, \quad (16) \end{aligned}$$

where  $f(\phi, \psi)$  is the distribution function of the angles  $\phi$  and  $\psi$ . If there is no magnetic fabric, then  $\phi$  has a uniform distribution over  $[0, \pi]$ . Neglecting a possible correlation between the directions of magnetic moments of the grains, the angle  $\psi$  is also distributed uniformly over  $[0, \pi]$ . As a consequence, for further estimations, we will assume that  $f(\phi, \psi) = 1$ .

To estimate the susceptibility measured from the thermodemagnetized state, consider the extreme case when the thermodemagnetization completely randomizes the direction of the interaction field in relation to the position of the grain easy axis. Physically, this happens when at blocking temperature  $T_b$  the interactions are weak, so the ratio  $\frac{E_0^i(\phi)}{k_B T_b} \ll 1$ . Then from eq. (16) and integrating over  $\psi$ , we obtain the expression of the magnetic susceptibility

$$\chi_T(H) = \frac{1}{2\pi} \int_0^\pi \frac{1}{2 \cos[2\theta_0(\phi)] + H \cos[\theta_0(\phi) - \phi]} d\phi. \quad (17)$$

The susceptibility of the completely thermodemagnetized state increases notably when the interaction field increases (Fig. 13a). The physical explanation to this increase lies in the fact mentioned earlier that the susceptibility increases with the increase of the interaction field  $H$  for the shallow potential well  $\pi/2 < \phi < \pi$ . Though for the

deep potential well  $0 < \phi < \pi/2$ , the susceptibility decreases, the overall effect favours the general increase of  $\chi_T(H)$ .

*AF-demagnetized state.* The application of AF forces the magnetic moment of a grain to switch from one direction to the other along its easy axis. In the absence of external or interaction fields, it leads to a total randomization of the magnetic moments for an SD ensemble when half of them falls in one direction and the second half falls in the opposite one. However, any magnetic field will break the symmetry making these states not equivalent. With the gradual decrease of the AF amplitude, the moment of the grain will finally be trapped in the biggest critical field state, that is, in the deepest potential well. Thus, even if the location of the magnetic moment before the AF treatment was in the shallow minimum  $\theta_0 = \theta_0^2$ , it will occupy eventually the deep potential well  $\theta_0 = \theta_0^1$ . Hence

$$\chi_{AF}(H) = \frac{1}{\pi} \int_0^{\pi/2} \frac{1}{2 \cos[2\theta_0(\phi)] + H \cos[\theta_0(\phi) - \phi]} d\phi. \quad (18)$$

The magnetic susceptibility of particles in AF-demagnetized state decreases when the interaction field increases (Fig. 13a). Physically, the decrease of  $\chi_{AF}$  is conditioned by the deepening of the potential well of the states with  $\theta_0 = \theta_0^1(\phi)$  when  $\phi < \pi/2$ , that is, when the direction of the interaction field is close to the direction of the magnetic moment. Such state interaction fields always decrease the magnetic susceptibility. Actually, the susceptibility increases sharply when a magnetic moment occupies the state  $\theta_0 = \theta_0^2(\phi)$ . So, the increase of  $\chi_T$  is secured namely by the occupation of this kind of states because of potential wells become shallower when  $\pi/2 < \phi < \pi$ , that is, when the direction of the interaction field is more or less opposite to the easy axis.

We measured the magnetic susceptibility after thermal demagnetization (560°C) and AF-demagnetization (200 mT along the core z-axis) for abnormal- and normal-fabric samples. Unfortunately, experimental Th-demagnetized state was difficult to obtain due to explosion of many samples during heating. Only 27 samples, 17 yielding abnormal fabrics and 10 yielding normal fabrics, were available at the end of experiments. As expected by the calculations, it can be seen in Fig. 13(b) that the susceptibility is stronger in the thermodemagnetized state than in AF-demagnetized state. We also note that normal-fabric samples yield a  $K$ -ratio in average lower than the abnormal-fabric samples.

### 5.1.3 Anisotropic distribution for the easy axes

If there is a magnetic fabric, then the easy axes are distributed non-homogeneously over the angles  $\psi$ , hence the distribution function  $f(\psi, \phi)$  is not constant. Let us suggest for simplicity that the distribution of interaction field vector is totally random so that  $f(\phi, \psi) = f(\psi)$ . We can formally decompose  $f(\psi)$  into Fourier series. Let us retain only the first two terms, so  $f$  becomes

$$f(\phi, \psi) = 1 + a \cos(2\psi), \quad (19)$$

where  $a$  is a coefficient. With this choice, the maximum susceptibility axis lies along  $\psi = 0$ .

*Thermodemagnetized state.* Using eq. (19), eq. (16) becomes

$$M = \frac{h}{8\pi} \int_{-\pi}^{\pi} \frac{2 - a \cos(2\theta_0(\phi))}{F} d\phi. \quad (20)$$

From here the susceptibility along  $\psi = 0$  direction is

$$K_1 = \frac{1}{4\pi} \int_0^\pi \frac{2 - a \cos(2\theta_0(\phi))}{F} d\phi \quad (21)$$

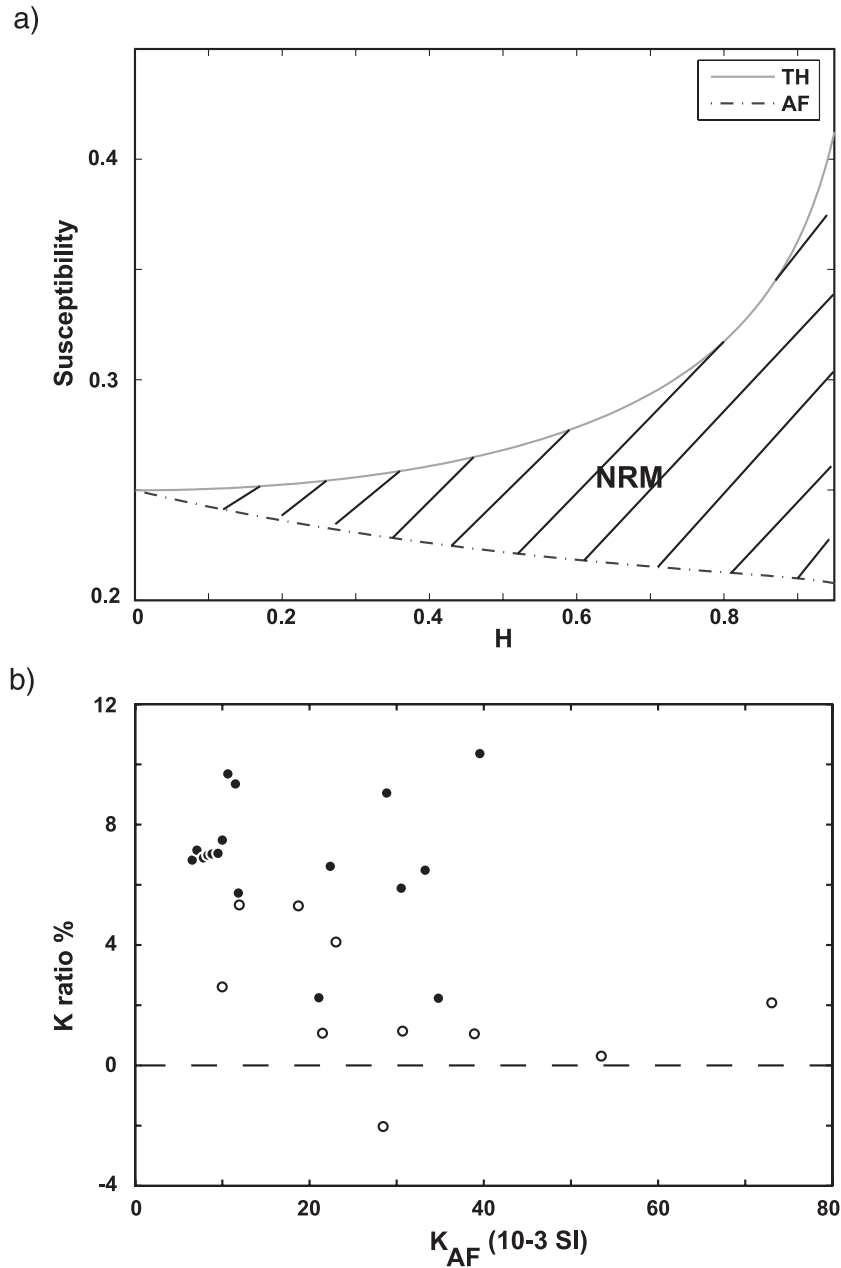


**Figure 13.** Influence of the interaction field on the bulk susceptibility. (a) Theoretical magnetic susceptibility of AF-demagnetized ( $K_{af}$ ) and thermodemagnetized ( $K_{th}$ ) globule cluster of SD grains as a function of the interaction field  $H$ . (b) Experimental value of bulk susceptibility for 17 abnormal-fabric samples (black circles) and 10 normal-fabric samples (white circles).  $K_{ratio}$  is the normalized difference in per cent between the bulk susceptibility after thermal demagnetization ( $K_{th}$ ) and after AF demagnetization ( $K_{af}$ ) such as  $K_{ratio} = [K_{th} - K_{af}]/K_{af} \times 100$ . As predicted by the model,  $K_{th}$  is always greater than  $K_{af}$  for all samples but one.  $K_{ratio}$  for the normal-fabric samples seems to be lower than those for the abnormal-fabric samples.

and along perpendicular axis

$$K_3 = \frac{1}{4\pi} \int_0^\pi \frac{2 + a \cos(2\theta_0(\phi))}{F} d\phi. \quad (22)$$

*AF-demagnetized state.* Using the same development, we calculate the minimal and maximal susceptibility for the AF-demagnetized particle.

$$K_1 = \frac{1}{2\pi} \int_0^{\frac{\pi}{2}} \frac{2 - a \cos(2\theta_0(\phi))}{F} d\phi \quad (23)$$

and along perpendicular axis

$$K_3 = \frac{1}{2\pi} \int_0^{\frac{\pi}{2}} \frac{2 + a \cos(2\theta_0(\phi))}{F} d\phi. \quad (24)$$

The anisotropy degree  $P = \chi_{max}/\chi_{min}$  decreases as the interaction field increases (Fig. 14a). Experimental value of the degree of anisotropy  $P$  have been measured for the same samples used in Fig. 13(b). Fig. 14(b) illustrates the comparison of the degree of anisotropy after thermal demagnetization and after AF demagnetization. The degree of anisotropy is, for all samples but two, stronger after AF demagnetization, in agreement with the outcome

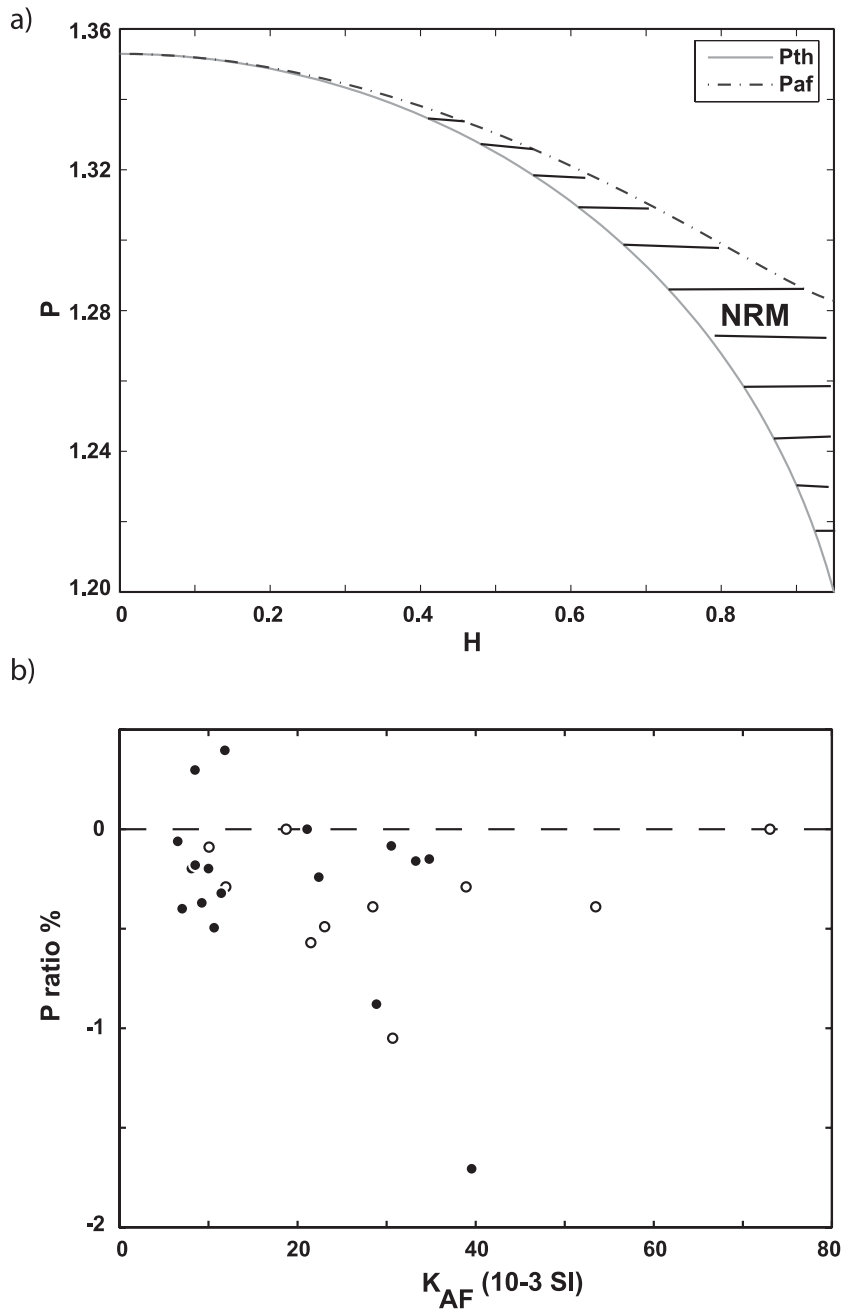


**Figure 14.** Influence of the interaction field on AMS anisotropy degree. (a) Theoretical AMS anisotropy degree  $P = K_1/K_3$  of AF-demagnetized and thermodemagnetized globule cluster of SD grains as a function of the interaction field  $H$ . The coefficient  $a$  of eq. (19) was taken as  $a = 1$ . (b) Experimental value of  $P$  for 17 abnormal-fabric samples (black circles) and 10 normal-fabric samples (white circles).  $P_{ratio}$  is the normalized difference in per cent between  $P$  measured after thermal demagnetization ( $P_{th}$ ) and after AF demagnetization ( $P_{af}$ ) such as  $P_{ratio} = [P_{th} - P_{af}]/P_{af} \times 100$ .  $K_{af}$  is the bulk susceptibility after AF demagnetization (SI unit). For most of the samples,  $P_{th}$  is always lower than  $P_{af}$  as predicted by the model. No different trends between  $P_{ratio}$  from abnormal- and normal-fabric samples are observed.

of the model. This model clearly shows that when interactions are relatively strong the anisotropy ellipsoid is approaching a sphere introducing noise in measurements. This can lead to abnormal fabrics.

## 5.2 Magnetic interactions at the origin of abnormal magnetic fabrics?

Several theoretical models have been developed to understand the effects of magnetic interactions on magnetic fabrics (Stephenson

1994; Cañón-Tapia 1996; Muxworthy & Williams 2004; Gaillot *et al.* 2006). All these models rely on a non-uniform distribution (lineation or foliation) of magnetic particles with uniaxial anisotropy. They predict that the degree of anisotropy is increased by magnetic interactions induced by the distribution anisotropy. On the contrary, the model by Cañón-Tapia (2001), which explores the influence of interacting and non-interacting magnetic fractions coexisting in the same sample, can predict in some particular cases a decrease of the degree of anisotropy for a significant interacting fraction. The present case is different as the non-uniform



distribution of the clusters corresponds to a lineation along plagioclase laths, but these clusters are built by SD particles with uniaxial anisotropy randomly distributed. The distance between two consecutive clusters is a few micrometres whereas magnetic particles building up these clusters are much closer. In this particular geometry, magnetic interactions are stronger within the cluster than between the clusters. If the lineation geometry was dominant, the AMS signal should increase along the flow direction but we observe the contrary: the AMS signal is noised in samples with abnormal fabrics, assuming an important part of interactions in spherical clusters.

Egli (2006a) have shown that densely packed interacting particles with uniaxial anisotropy also interfere with the remanent magnetization. In our study, the A-ARM is well defined for lava flows yielding normal AMS fabric, which seems to be the case when interactions are small. On the contrary, the A-ARM is less well defined for lava flows with abnormal AMS fabric. Principal axes seem to be rotated with respect to samples yielding a normal fabric. Magnetostatic interactions may also explain this difference on magnetic remanence between the two groups.

### 5.3 Alternative interpretations

Borradaile & Gauthier (2001) have shown that AMS fabric might be complicated by the mixture of inverse and normal AMS fabrics from SD and MD titanomagnetite. To avoid this kind of complication, they recommend to remove samples with high susceptibility. In our study, samples yielding normal or abnormal fabrics do not present a significant difference on bulk susceptibility (Table 1), therefore this is not the explanation in our case. An other alternative interpretation calls for a particular strain pattern in which the main force would be horizontal yielding a vertical lineation. Such pattern can be encountered at the flow front, for straight or divergent flow producing a discrepancy between flow direction and magnetic fabrics (Merle 1998), or at the last stage of flow emplacement when the lava is quite viscous and thus resists to the flow. Such horizontal stress is able to produce abnormal AMS fabric with regard to the mean flow but normal fabric in agreement with the local strain. The local flow direction deduced from the LPO analyses on plagioclases show a good agreement with the mean flow direction in cases of normal and abnormal AMS fabrics. Furthermore, the analyses of the remanent fabric tallies with the LPO of plagioclases in both cases. So this direct relation which exists between the magnetic fabric and the crystallographic fabrics tends to rule out this hypothesis.

Other abnormal orientations can be found far from the flow boundaries as the result of the cyclic movement of particles (Cañón-Tapia & Chávez-Álvarez 2004). From a simple numerical modelling, these authors showed that the abnormal orientations would depend on both the elongation ratio of the particles and the amount of shear that is sampled. Such dependence on particle shape is important in the present context because it indicates that, at least theoretically, two sets of particles with different aspect ratios may have their abnormal orientation at different places in the flow. The possibility of having subfabrics could explain why the plagioclases have a normal crystallographic fabric while AMS fabric is abnormal. Unfortunately, a check of this model requires a particular sampling along several different profiles, which is not the case in this study. However, we do not believe that this model can account for our measurements because we observed trains of globular aggregates along the silicate microlithe framework that suggest strong magnetic interactions. We have shown that the magnetic interaction

fields induced by these globular aggregates could introduce noise in the AMS measurement by decreasing the degree of anisotropy.

Finally, particle clusters identified in abnormal fabrics (Fig. 1) seem to result from a late crystallization in the lava of Fe-Ti oxides, by destabilization of the interstitial glass. Two cases have to be distinguished. Horizontal strain would deform the magnetic clusters and alter the orientation of plagioclases if the late crystallization occurred during the phase where the lava is viscous. We did not observe however such deformation. The second case corresponds to the crystallization of magnetic clusters just after the lava stopped to flow. Hargraves *et al.* (1991) has shown that, even when no early microphenocrysts of titanomagnetites were formed, AMS is an indirect reflection of the pre-existing silicate fabric by distribution anisotropy of late crystallized particles along the silicate fabric in absence of stress. This is the case in our study where the clusters are aligned along the plagioclase framework and yet, abnormal AMS fabrics are uncorrelated with LPO of plagioclases. This process of late crystallization is also not suitable to explain the observed abnormal fabrics.

## 6 CONCLUSIONS

This study brings us to the following conclusions:

(1) A multiscale approach is recommended to determine the flow direction of the Kerguelen flood basalts. We have shown that the flow direction can be retrieved from AMS analysis with the help of EBSD analyses on plagioclases LPO, these later can be performed from a single sample by flow. In this study, the analysis of the magnetic fabric at the flow scale allows to distinguish between normal and abnormal fabrics. Then, analysis at the whole-section-scale is important to strengthen the conclusions. We found that the flow direction obtained from the stack of all normal magnetic fabrics is consistent with the geological observations. This supports Henry *et al.* (2003) and Plenier *et al.* (2005)'s conclusions that, at least for the volcanism encountered in Kerguelen, several successive lava flows emplaced under similar conditions have to be analysed altogether.

(2) Experimental evidences show that our samples yielding abnormal fabrics seem to be linked to a predominance of SD interacting grains (low-Ti titanomagnetite) associated in micrometric globules and crystallized in the interstitial glass along the plagioclase laths.

(3) Our preferred interpretation to account for abnormal fabrics in these lavas relies on the influence of magnetic interactions. Our model predicts that the degree of anisotropy decreases as the magnetic interactions increase. Thus, we think that a large scattering in magnetic fabric, which led in the present case to abnormal mean fabrics, could be explained by strong magnetic interactions in a particular arrangement of densely packed magnetic particles.

## ACKNOWLEDGMENTS

We are grateful to the 'Institut Polaire Paul Emile Victor' for providing transport facilities and support for this project. We thank Alain Vauchez for scientific discussions, Guillaume Plenier for his help during the preliminary AMS measurements and Thierry Poidras and Patrick Nicol for technical help during laboratory experiments. We thank Christophe Nevado for preparing the thin polished sections. FORCs analyses have been performed at the CEREGE laboratory, Aix en Provence (France). Pierre Rochette is gratefully acknowledged. We are grateful to M. Winklhofer and an anonymous referee whose valuable comments and remarks significantly helped

improving the text and the data presentation. The editorial work of E. Apple is also appreciated.

## REFERENCES

- Arbaret, L., Diot, H. & Bouchez, J.L., 1996. Shape fabrics of particles in low concentration suspensions: 2D analogue experiments and application to tilting in magma, *J. Struct. Geol.*, **18**, 941–950.
- Bascou, J., Camps, P. & Dautria, J.M., 2005. Magnetic versus crystallographic fabrics in a basaltic lava flow, *J. Volc. Geotherm. Res.*, **145**, 119–135.
- Borradaile, G.J. & Gauthier, D., 2001. AMS-detection of inverse fabrics without AARM in ophiolite dikes, *J. geophys. Res.*, **28**, 3517–3520.
- Bunge, H.J., 1958. *Texture Analysis in Material Sciences*, Butterworths, London.
- Camps, P., Henry, B., Nicolaysen, K. & Plenier, G., 2007. Statistical properties of paleomagnetic directions in Kerguelen lava flows: implications for the late Oligocene paleomagnetic field, *J. geophys. Res.*, **112**, B06102, doi:10.1029/2006JB004648.
- Cañón-Tapia, E., 1996. Single-grain distribution anisotropy: a simple three-dimensional model, *Phys. Earth planet. Inter.*, **94**, 117–131.
- Cañón-Tapia, E., 2001. Factors affecting the relative importance of shape and distribution anisotropy in rocks: theory and experiments, *Tectonophysics*, **340**, 117–131.
- Cañón-Tapia, E. & Chávez-Álvarez, M.J., 2004. Theoretical aspects of particle movement in flowing magma: implication for the anisotropy of magnetic susceptibility of dykes and lava flows, *Geol. Soc. Lond. Spec. Pub.*, **238**, 227–249, doi:10.1144/GSL.SP.2004.238.01.15.
- Cañón-Tapia, E. & Pinkerton, H., 2000. The anisotropy of magnetic susceptibility of lava flows: an experimental approach, *J. Volc. Geotherm. Res.*, **98**, 219–233.
- Cañón-Tapia, E., Walker, G.P.L. & Herrero-Bervera, E., 1996. The internal structure of lava flows—insights from AMS measurements: I. Near-vent a’a, *J. Volc. Geotherm. Res.*, **70**, 21–36.
- Cañón-Tapia, E., Walker, G.P.L. & Herrero-Bervera, E., 1997. The internal structure of lava flows—insights from AMS measurements: II. Hawaiian pahoehoe, toothpaste lava and ‘a’ā, *J. Volc. Geotherm. Res.*, **76**(1–2), 19–46.
- Cisowski, S., 1981. Interacting vs. non-interacting single domain behavior in natural and synthetic samples, *Phys. Earth planet. Inter.*, **26**, 56–62.
- Constable, C. & Tauxe, L., 1990. The bootstrap for magnetic susceptibility tensor, *J. geophys. Res.*, **95**, 83–95.
- Dunlop, D., 1983. Viscous magnetization of 0.04–100  $\mu\text{m}$  magnetites, *Geophys. J. R. astr. Soc.*, **74**, 667–687.
- Dunlop, D.J. & Özdemir, O., 1997. *Rock Magnetism: Fundamentals and Frontiers*, Cambridge University Press, Cambridge.
- Egli, R., 2006a. Theoretical considerations on the anhysteretic remanent magnetization of interacting particles with uniaxial anisotropy, *J. geophys. Res.*, **111**, B12S18, doi:10.1029/2006JB004577.
- Egli, R., 2006b. Theoretical aspects of dipolar interactions and their appearance in first-order reversal curves of thermally activated single-domain particles, *J. geophys. Res.*, **111**, B12S17, doi:10.1029/2006JB004567.
- Evans, M.E., Krása, D., Williams, W. & Winklhofer, M., 2006. Magnetostatic interactions in a natural magnetite-ulvöspinel system, *J. geophys. Res.*, **111**, B12S16, doi:10.1029/2006JB004454.
- Fanjat, G., Shcherbakov, V. & Camps, P., 2012. Influence of magnetic interactions on the anisotropy of magnetic susceptibility: the case of single domain cluster aggregation, *Stud. Geophys. Geod.*, **56**(2), in press.
- Florez, J., Mazo-Zuluaga, J. & Restrepo, J., 2005. Ferrimagnetic to paramagnetic transition in magnetite: Mössbauer versus monte carlo, *Hyperfine Interact.*, **161**(1), 161–169.
- Gaillot, P., de Saint Blanquat, M. & Bouchez, J.L., 2006. Effects of magnetic interactions in anisotropy of magnetic susceptibility: models, experiments and implications for igneous rock fabrics quantification, *Tectonophysics*, **418**, 3–19.
- Greenwood, N.N. & Gibb, T.C., 1971. *Mössbauer Spectroscopy*, Chapman and Hall, London.
- Gunnlaugsson, H.P., Helgason, Ö., Kristjánsson, L., Nørnberg, P., Rasmussen, H., Steinthorsson, S. & Weyer, G., 2006. Magnetic properties of olivine basalt: application to Mars., *Phys. Earth planet. Inter.*, **154**(3–4), 276–289.
- Gunnlaugsson, H.P., Rasmussen, H., Kristjánsson, L., Steinthorsson, S., Helgason, Ö., Nørnberg, P., Madsen, M.B. & Mørup, S., 2008. Mössbauer spectroscopy of magnetic minerals in basalt on earth and mars, *Hyperfine Interact.*, **182**, 87–101.
- Hargraves, R.B., Johnson, D. & Chan, C., 1991. Distribution anisotropy: the cause of AMS in igneous rocks? *Geophys. Res. Lett.*, **18**, 2193–2196.
- Henry, B., Plenier, G. & Camps, P., 2003. Post-emplacement tilting of lava flows inferred from magnetic fabric study: the exemple of Oligocene lavas in the Jeanne d’Arc Peninsula (Kerguelen Islands), *J. Volc. Geotherm. Res.*, **127**, 153–164.
- Hext, G., 1963. The estimation of second order tensor with related tests and design, *Biometrika*, **50**, 153–173.
- Jelinek, V., 1976. The statistical theory of measuring anisotropy of magnetic susceptibility of rocks and its application, *Geofisika, Brno, Spec. Publ.*, 1–88.
- Jelinek, V., 1978. Statistical processing of magnetic susceptibility measured on groups of specimens, *Stud. Geophys. Geod.*, **22**, 50–62.
- Jelinek, V., 1981. Characterization of the magnetic fabric of rocks, *Tectonophysics*, **79**, 63–67.
- Khan, M., 1962. The anisotropy of magnetic susceptibility of some igneous and metamorphic rocks., *J. geophys. Res.*, **67**, 2873–2885.
- Knight, M. & Walker, G., 1988. Magma flow directions in dikes of the Koolau Complex, Oahu, determined from magnetic fabric studies, *J. geophys. Res.*, **93**, 4301–4319.
- Krieger-Lassen, N., 1996. The relative precision of crystal orientations measured from electron backscattering patterns, *J. Microsc.*, **181**, 72–81.
- Linder, J. & Leonhardt, R., 2009. Paleomagnetic full vector record of four consecutive mid miocene geomagnetic reversals, *Phys. Earth planet. Inter.*, **177**, 88–101.
- Merle, O., 1998. Internal strain within lava flows from analogue modelling, *J. Volc. Geotherm. Res.*, **81**, 189–206.
- Muxworthy, A. & Williams, W., 2004. *Geol. Soc. Lond. Spec. Pub.*, **238**, 37–47, doi:10.1144/GSL.SP.2004.238.01.04.
- Nougier, J., 1970a. Contribution a l’étude géologique et géomorphologique des îles Kerguelen, *C.N.F.R.A.*, **27**, 440 and 256pp, 2 tomes.
- Nougier, J., 1970b. *Terres Australes et Antarctique Françaises (T.A.A.F.)*, Kerguelen Islands reconnaissance map, 1:200 000, Institut. Geograph. Nat’l, Paris.
- O’Reilly, W., 1984. *Rock and Mineral Magnetism*, Blackie, Glasgow.
- Pike, R.P., Roberts, A.P. & Verosub, K.L., 1999. Characterizing interactions in fine magnetic particle systems using first order reversal curves, *J. appl. Phys.*, **85**, 6660–6667.
- Plenier, G., Camps, P., Henry, B. & Nicolaysen, K., 2002. Paleomagnetic study of Oligocene (24–30 Ma) lava flows from the Kerguelen Archipelago (southern Indian Ocean): directional analysis and magnetostratigraphy, *Phys. Earth planet. Inter.*, **133**, 127–146.
- Plenier, G., Camps, P., Henry, B. & Ildefonse, B., 2005. Determination of flow directions by combining AMS and thin-section analyses: implications for Oligocene volcanism in the Kerguelen Archipelago (southern Indian Ocean), *Geophys. J. Int.*, **160**, 63–78.
- Potter, D.K. & Stephenson, A., 1988. Single-domains particles in rocks and magnetic fabric analysis, *Geophys. Res. Lett.*, **15**, 1097–1100.
- Prévot, M., 1981. Some aspects of magnetic viscosity on subaerial and submarine volcanic rocks, *Geophys. J. R. astr. Soc.*, **66**, 169–192.
- Rivas-Sanchez, M., Alva-Valdivia, L., Arenas-Alatorre, J., Urrutia-Fucugauchi, J., Perrin, M., Goguitchaichvili, A., Ruiz-Sandoval, M. & Molina, M.A.R., 2009. Natural magnetite nanoparticles from an iron-ore deposit: size dependence on magnetic properties, *Earth Planets Space*, **61**, 151–160.
- Roberts, A., Pike, R. & Verosub, K., 2000. First order reversal curve diagrams: a new tool for characterizing the magnetic properties of natural sample, *J. geophys. Res.*, **105**, 28461–28475.
- Rochette, P., Aubourg, C. & Perrin, M., 1999. Is this magnetic fabric normal? a review and case studies in volcanic formations, *Tectonophysics*, **307**, 219–234.

- Roggwiler, P. & Kundig, W., 1973. Mössbauer spectra of superparamagnetic Fe<sub>3</sub>O<sub>4</sub>, *Solid State Commun.*, **12**, 901–903.
- Schmidt, N.H. & Olesen, N., 1989. Computer-aided determination of crystal-lattice orientation from electron-channeling patterns in the SEM, *Can. Mineral.*, **27**, 15–22.
- Senanayake, W. & McElhinny, M., 1982. The effects of heating on low-temperature susceptibility and hysteresis properties of basalts, *Phys. Earth planet. Inter.*, **30**, 317–321.
- Shcherbakov, V.P. & Shcherbakova, V., 1975. On the magnetostatic interaction in a system of single-domain grains, *Izv. Earth Phys.*, **9**, 101–104.
- Stephenson, A., 1994. Distribution anisotropy: two simple models for magnetic lineation and foliation, *Phys. Earth planet. Inter.*, **25**, 49–53.
- Tarling, D.H. & Hrouda, F., 1993. *The Magnetic Anisotropy of Rocks*, Chapman and Hall, London.
- Theillier, E. & Theillier, O., 1944. Recherches géomagnétiques sur les coulées volcaniques d'auvergne, *Ann. Geophys.*, **1**, 37–52.
- Thompson, A., Rancourt, D.G., Chadwick, O.A. & Chorover, J., 2011. Iron solid-phase differentiation along a redox gradient in basaltic soils, *Geochim. Cosmochim. Acta*, **75**(1), 119–133.
- Torquato, S., Truskett, T.M. & Debenedetti, P.G., 2000. Is random close packing of spheres well defined? *Phys. Rev. Lett.*, **81**, 2064–2067.
- Vanalboom, A., Degraeve, E. & Vandenberghe, R.E., 1994. Crystal-field interpretation of the temperature-dependence of the Fe-57 Mössbauer quadrupole splitting in 2 orthopyroxenes, *Hyperfine Interact.*, **91**(1–4), 703–707.
- Wenk, H.R., Joswig, W., Tagai, T., Korekawa, M. & Smith, B.K., 1980. The average structure of an 62-64 labradorite, *Am. Miner.*, **65**, 81–95.
- Winklhofer, M. & Zimany, G.T., 2006. Extracting the intrinsic switching field distribution in perpendicular media: a comparative analysis, *J. appl. Phys.*, **29**, 595–596.
- Wohlfarth, E.P., 1958. Relations between different modes of acquisition of remanent magnetization of ferromagnetic particles, *J. appl. Phys.*, **99**(8), doi:10.1063/1.2176598.
- Yang, H.J., Frey, F.A., Weiss, D., Giret, A., Pyle, D. & Michon, G., 1998. Petrogenesis of the flood basalts forming the Northern Kerguelen Archipelago: implications for the Kerguelen plume, *J. Petrol.*, **99**, 711–748.
- Zhou, W., der Voo, R.V. & Peacor, D.R., 1997. Single-domain and superparamagnetic titanomagnetite with variable Ti content in young ocean-floor basalts: no evidence for rapid alteration, *Earth planet. Sci. Lett.*, **150**, 353–362.